Micro and Nanostructures 206 (2025) 208220

Contents lists available at ScienceDirect

Micro and Nanostructures

journal homepage: www.journals.elsevier.com/micro-and-nanostructures

Optimizing world-record thin-film ACIGS solar cells with innovative 'hockey stick'-shaped GGI profile for tandem solar technology

Nour El I Boukortt [a,b,*], Antonio Garcia Loureiro [a]

[a] Centro Singular de Investigación en Tecnoloxías Intelixentes (CiTIUS), University of Santiago de Compostela, Santiago de Compostela, Spain
[b] Department of Electronics and Information Systems, Ghent University, Technology Park 126, Zwijnaarde, Belgium

ARTICLE INFO

Keywords:
Thin-film
Deposition techniques
ACIGS
Defect density
Interfaces

ABSTRACT

In this study, we perform a comprehensive optimization of key parameters influencing the performance of ACIGS (Ag-doped Cu(In,Ga)Se_2) solar cells, focusing on the effects of deposition environment and techniques. Parameters such as absorber thickness, dopant concentration, electron affinity, bulk defect density, and interface trap density are analyzed using advanced TCAD simulations. A calibrated device model based on experimental data accounts for all relevant material properties and defect distributions. Our findings reveal that minimizing bulk and interface defects primarily induced by deposition conditions is critical to enhancing stability and performance. Under standard test conditions (AM1.5G, 25 °C), the reference and optimized ACIGS single-junction cells achieve power conversion efficiencies (PCEs) of 23.60 % and 25.80 %, respectively. Furthermore, under varying temperatures (20–90 °C) and illumination intensities (10–120 mW/cm^2), the optimized cell demonstrates notable improvements: a 15 % enhancement in power temperature coefficient and a 22 % increase in voltage temperature coefficient. For tandem configurations, we pair the optimized ACIGS bottom cell featuring a double gallium grading profile with a perovskite top cell (bandgap ≈ 1.70 eV). This results in PCEs of 31.92 % and 32.39 % for tandem devices using ITO and band-to-band tunneling (B2BT) interconnections, respectively, under AM1.5G illumination. The results are benchmarked against recent studies, providing valuable insights into advanced strategies and the physical behavior of high-efficiency tandem perovskite/ACIGS solar cells.

1. Introduction

Since Han et al. synthesized chalcopyrite $CuInSe_2$ in 1953, CIGS (Copper Indium Gallium Selenide) has been progressively implemented in solar cells, achieving power conversion efficiencies (PCE) greater than 23 % in single-junction devices [1–4]. In early 2024, Uppsala University announced a record conversion efficiency of 23.64 % for a thin-film Ag–Cu($In_{1-x}Ga_x$)Se_2 solar cell. This achievement was made possible by employing a "hockey stick"-shaped gallium gradient profile, featuring a constant gallium (Ga) content in the upper half of the absorber and a higher concentration near the back contact, which effectively minimized voltage (V_{oc}) losses. ACIGS stands for Ag–Cu–In–Ga–Se_2, a modified version of the conventional CIGS (Cu–In–Ga–Se_2) absorber material [4]. This

* Corresponding author. Centro Singular de Investigación en Tecnoloxías Intelixentes (CiTIUS), University of Santiago de Compostela, Santiago de Compostela, Spain.
E-mail address: nourelislam.boukortt@rai.usc.es (N. El I Boukortt).

https://doi.org/10.1016/j.micrna.2025.208220
Received 11 March 2025; Received in revised form 22 April 2025; Accepted 20 May 2025
Available online 23 May 2025

design incorporated a significant amount of silver (Ag) into the absorber layer, while reducing the CdS buffer thickness to 25 nm, which improved light absorption and boosted efficiency [4]. In 2019, Solar Frontier (SF) reached an efficiency of 23.35 % by introducing sulfur to the front surface of the CIGS absorber. This modification resulted in a gradual lowering of the valence band minimum and an increase in the bandgap energy (E_g). Consequently, the hole concentration at the heterojunction decreased, leading to an increase in the open circuit voltage (V_{oc}) [5,6]. The performance of CIGS solar cells is significantly influenced by factors such as absorber layer thickness, dopant concentration, and the gallium composition grading profile [7–9]. CIGS features a tunable bandgap ranging from 1.0 to 1.7 eV, which can be adjusted by varying the Ga/(In + Ga) ratio, making it suitable for both single-junction and tandem applications [8,10]. A CIGS thickness of 2–3 μm is commonly employed to ensure effective light absorption. Recent advancements in high-efficiency CIGS-based solar cells on flexible substrates have expanded their potential for applications like building-integrated photovoltaics (BIPV). These developments also show promises for reducing production costs through roll-to-roll manufacturing processes [11,12].

CIGS solar cell fabrication begins with the deposition of the electrical back contact layer onto the substrate, which serves as the foundation for the subsequent layers [4,12]. This is typically followed by the deposition of the absorber and buffer layers and finally completed with the coating of the window layer [4,12]. The window layer, often deposited using vacuum-based deposition methods such as sputtering or evaporation, plays a crucial role in allowing light to enter the cell while minimizing reflection and absorption losses. The n-type buffer layer, which is essential for forming the p-n junction, can be coated using both vacuum (e.g., chemical vapor deposition, CVD) and non-vacuum techniques (e.g., chemical bath deposition, CBD) [4,11]. These processes ensure the formation of high-quality interfaces necessary for optimal solar cell performance [4]. Ongoing research continues to focus on improving material properties, interface engineering, and design configurations to further enhance the efficiency of CIGS cells [8,10,12].

This study focuses on the numerical optimization of the ACIGS device using Silvaco TCAD tools. It examines how the properties of individual layers (window, buffer, and absorber) influence device performance, specifically in terms of improving light trapping and reducing transmission losses. The ACIGS device was calibrated based on a fabricated model, considering material properties and

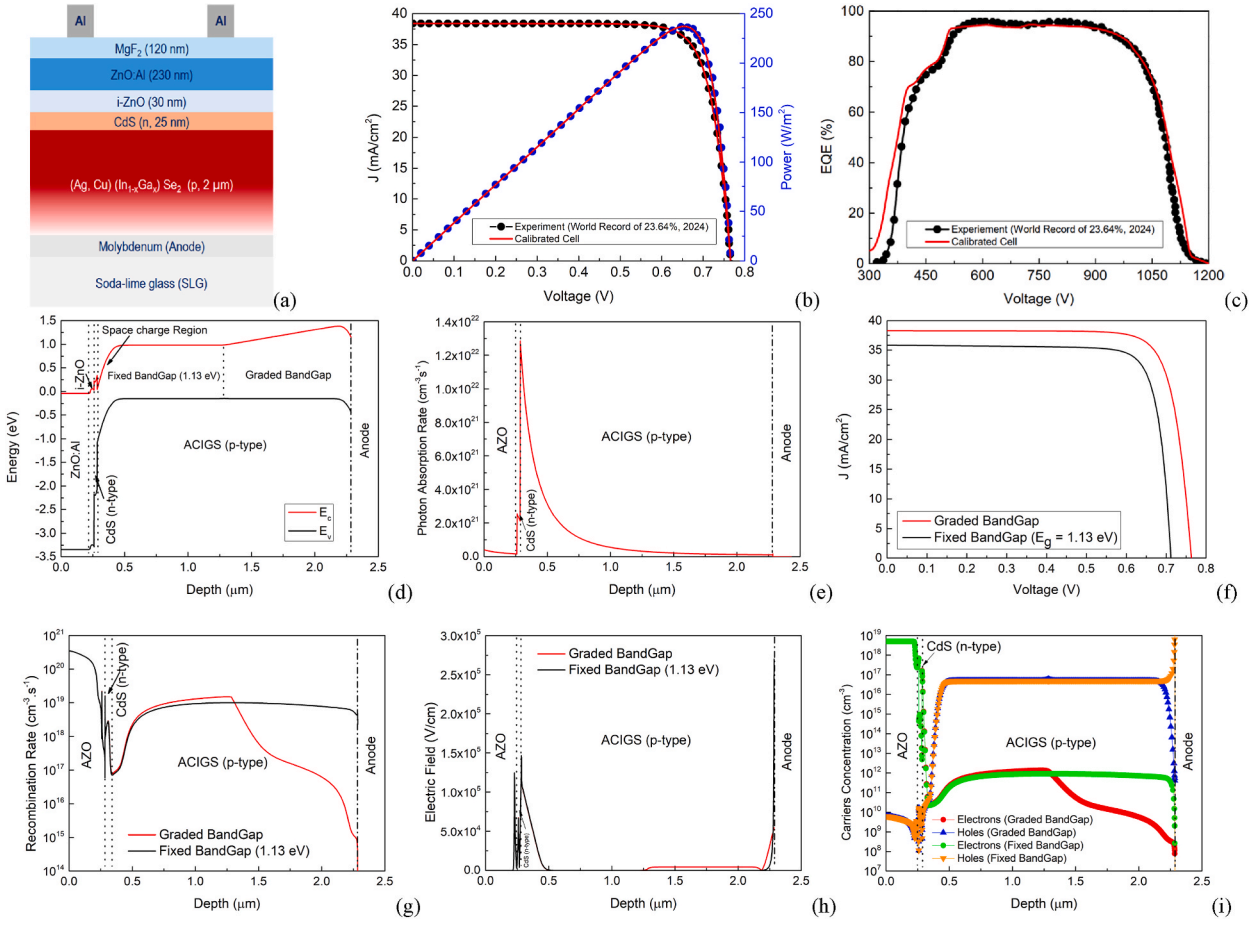

Fig. 1. (a) Cross-sectional of ACIGS solar cell model. (b) J–V and power curves of the calibrated and fabricated models. (c) EQE spectrum the calibrated and fabricated models. (d) Corresponding energy band. (e) Photogeneration rate across the cell. (f) J–V curves for fixed bandgap profile and 'hockey stick'-shaped GGI profile. (g) Recombination rate for fixed bandgap profile and 'hockey stick'-shaped GGI profile. (h) Electric field across ACIGS structure. (i) Electron/Hole concentration for fixed bandgap profile and 'hockey stick'-shaped GGI profile.

defects at both the interfaces and within the bulk of the cells [4]. Key parameters such as thickness, dopant concentration, electron affinity, bulk defect density, and interface trap density were investigated to assess their impact on performance. It was found that the interface trap density at the front side (CdS/ACIGS interface) plays a critical role in chemical passivation, with lower defect densities being essential to minimizing recombination losses. These losses are influenced by the deposition techniques and conditions used during fabrication, emphasizing the need for careful consideration of the quality of each layer. Various thin-film deposition techniques, such as co-evaporation [13], physical vapor deposition (PVD) [14], pulsed laser deposition (PLD) [15], chemical vapor deposition (CVD) [16], metal-organic chemical vapor deposition (MOCVD) [17], electron beam deposition (EBD) [18], molecular beam epitaxy (MBE) [19], and sputtering [20,21], have been employed, each offering specific advantages and challenges. A thorough evaluation of these methods is critical for optimal cell growth. These features are promising for tandem solar cell (TSC) configurations [22]. Both reference and optimized cells were tested under varying temperatures and light intensities, allowing for the extraction of power and voltage temperature coefficients. Notably, efficiencies surpassing 25 % were attained under simulated conditions, showcasing the potential of optimized ACIGS cells.

From recent key research findings, we conduct a detailed numerical investigation of two-terminal (2T) perovskite/ACIGS tandem solar cells using Silvaco TCAD tools, focusing on their electrical and optical performance [10,22]. The tandem device structures feature two distinct interconnection methods: band-to-band tunneling (B2BT) and series connection via indium tin oxide (ITO) [10]. In both configurations, the optimized ACIGS device serves as the bottom subcell. The results are compared with recent literature, highlighting the ongoing challenges in achieving high-efficiency thin-film tandem photovoltaics [10,22]. This study emphasizes the critical role of material selection and precise design strategies in advancing the efficiency limits of perovskite/ACIGS tandem solar cells.

2. Device simulation

2-D simulations were performed based on the fabricated device reported by Keller et al. [4] using Silvaco 2D under room temperature, dark, and AM1.5 illumination conditions. This device represents the latest advancements in achieving record research device efficiency, introducing a new record efficiency of 23.6 % for ACIGS solar cells. The global model structure used for the ATLAS 2D simulations of ACIGS solar cells is presented in Fig. 1(a) and consists of the following configuration from top to bottom: Front contact (Al)/Al–ZnO/i-ZnO/CdS/ACIGS/Rear contact (Molybdenum)/Soda-Lime Glass (SLG). The ACIGS structure includes a soda-lime glass (SLG) substrate, a 290 nm molybdenum (Mo) back contact deposited by DC magnetron sputtering, and a 10 nm sodium fluoride (NaF) precursor layer applied through thermal evaporation to passivate the Mo back contact [4]. This thin, uniform NaF layer reduces surface defects and traps, thereby enhancing the electrical properties of the Mo layer and minimizing recombination losses at the Mo/ACIGS interface, which is crucial for improving the solar cell's efficiency [4]. Among various substrate types, soda-lime glass has proven to be the most suitable, as it better matches the molybdenum back contact in terms of thermal expansion coefficient. Additionally, sodium (Na) diffusion from the SLG (through the Mo layer) into the CIGS absorber layer significantly benefits overall cell performance. This effect is mainly attributed to the passivation of grain boundary defects, increased carrier density, and changes in crystal orientation due to the incorporation of sodium in the CIGS layer [4,23]. The simulation did not account for the influence of the SLG substrate on the heterojunction band energy layout due to limitations of the software used in this study. Molybdenum thin film is chosen as the back contact because of its chemical inertness, good thermal stability, suitable electrical and optical properties (including reflectivity), and favorable ohmic characteristics with the CIGS absorbing layer (resulting from $MoSe_2$ layer formation during the selenization step) [24]. The work function of the Mo back contact was set at 5.65 eV [1]. Surface recombination under the contacts is assumed to be very high, at 10^7 cm^2/V·s. As a result, the majority carrier barrier height at the Mo/absorber interface varies based on the different values of the bandgap and electron affinity of the absorber layer, as described in Equation (1) below [25]:

$$\Phi_{Bp} = E_g - \Phi_{Bn} \tag{1}$$

where E_g is the bandgap of the absorber layer, and Φ_{Bn} is the minority carrier barrier height, defined by Equation (2) as follow [26].

$$\Phi_{Bn} = \Phi_{Mo} - \chi_s \tag{2}$$

Φ_{Mo} represents the work function of the molybdenum metal, while χ_s denotes the electron affinity of the absorber layer.

The absorber layer comprises a 2.0–2.1 μm thick ACIGS film, fabricated using a three-stage co-evaporation process (In-poor → In-rich → In-poor) at a maximum temperature of approximately 530 °C [4]. This process results in a 'hockey stick'-shaped GGI profile. To facilitate grain growth during fabrication, a substantial amount of silver (Ag) is incorporated into the $Cu(In,Ga)Se_2$ (CIGS) thin films. After the ACIGS deposition, a 3–5 nm rubidium fluoride (RbF) layer is applied at 350 °C without breaking the vacuum, ensuring cleanliness and enhancing interface quality [4]. Subsequently, a ~25 nm cadmium sulfide (CdS) buffer layer is deposited at 60 °C via chemical bath deposition [4]. The cell is completed with a ~30 nm intrinsic zinc oxide (i-ZnO) layer, a 230 nm aluminum-doped zinc oxide (Al–ZnO) layer, and a 110 nm magnesium fluoride (MgF_2) anti-reflection coating (ARC) layer [4]. The work function of the aluminum front electrode was set to 4.70 eV which can help achieve ohmic contact with the n-ZnO TCO layer.

The J–V curves for the calibrated and fabricated ACIGS models are shown in Fig. 1(b). These curves depict the current density values corresponding to different voltage levels, demonstrating favorable electrical behavior at room temperature. Fig. 1(c) presents the external quantum efficiency (EQE) of the ACIGS models, indicating favorable optical behaviour. Fig. 1(d) shows the band diagram in a 'hockey stick'-shaped GGI profile at J_{sc} conditions. Fig. 1(e) presents photo absorption rate across the cell. Fig. 1(f) presents the J–V curves, highlighting the performance advantage of the graded bandgap profile over the fixed bandgap profile. A significant increase was observed in the J_{sc} of 2.31 mA/cm^2 and in V_{oc} of 60.55 mV were obtained. This improvement is further supported by Fig. 1

(g), which demonstrates a reduction in carrier recombination in the first half of the graded absorber layer. Fig. 1(h) illustrates the increase in the electric field in the first half of the graded absorber layer, which helps prevent carrier recombination rather than causing it. This is supported by Fig. 1(i), which shows a reduction in minority carrier (electron) concentration in the first half of the graded absorber layer, indicating that the enhanced electric field effectively drives carriers apart, minimizing recombination and improving device performance. The material properties used in the ACIGS structure were derived from experimental studies and our previous investigations [1,4,5]. These values are summarized in the supplementary material (Table S1). Additionally, Table 1 presents a detailed comparison between the measured and simulated output characteristics, highlighting the model's accuracy.

3. Results and discussions

This research primarily focuses on enhancing the conversion efficiency of thin-film ACIGS solar cells by exploring various approaches related to the electrical properties of the window, buffer, and absorber layers. We analyzed key trends in ACIGS solar cell parameters, focusing on mechanisms involving defect density and interface defect density. This study also provides valuable insights for optimizing the design and accurate characterization of a complete solar cell structure, supporting the advancement of high-performance ACIGS-based devices.

3.1. Window layer optimization

Zinc oxide (ZnO) is an II-VI compound semiconductor characterized by a wurtzite crystal structure [27,28]. ZnO is primarily an n-type semiconductor, often forming large single crystals, which offers the benefit of a less defect concentration [27–29]. However, controlling ZnO's conductivity remains challenging, as even minimal defect and impurity concentrations (as low as 10^{14} cm^{-3} or 0.01 ppm) can significantly impact its electrical and optical properties [27–31]. ZnO is widely used for transparent conductive oxide (TCO) material, with an electron mobility (μ_n) ranging from 130 to 440 cm^2/V.s and a hole mobility (μ_P) between 0.1 and 50 cm^2/V.s [32]. Aluminum-doped zinc oxide (Al–ZnO or AZO) is a TCO created by incorporating aluminum (Al) into the zinc oxide structure. This doping significantly enhances the electrical conductivity of ZnO while maintaining its optical transparency, making AZO valuable for various applications. Other group III elements, including boron (B), gallium (Ga), and indium (In), can also serve as dopants in ZnO [33]. Undoped ZnO has an electron affinity of 4.35 eV and a direct bandgap energy of 3.28 eV, with an electron concentration around 10^{17} cm^{-3}. In contrast, heavily doped AZO and Ga-doped ZnO (GZO) achieve low resistivity with electron concentrations in the range of 10^{20} to 10^{21} cm^{-3}. Reported resistivities for AZO and GZO are approximately 8.5×10^{-5} Ω cm and 8.1×10^{-5} Ω cm, respectively, comparable to 7.7×10^{-5} Ω cm for indium tin oxide (ITO) [34]. Additionally, AZO and GZO offer higher transparency, improved thermal stability, and lower growth temperatures, making them promising alternatives [35,36]. Doping ZnO with gallium (Ga) is particularly effective for enhancing conductivity. GZO acts as a direct wide bandgap semiconductor, with its high electron concentration resulting from Ga substituting for Zn (GaZn). This substitution introduces donor defects, as the energy level associated with GaZn is just 0.1 eV below the conduction band minimum of ZnO. Fig. 2 illustrates how n-type dopant concentration affects cell performance. Increasing the dopant concentration (when its above 10^{19} cm^{-3}) can enhance the collection of photogenerated carriers, leading to improved electrical efficiency. The AZO doping concentration influences not only the Fermi energy level (E_F) but also parameters like electron affinity (χ), as shown in Fig. 3, which depicts efficiency dependent on electron affinity [37].

ZnO-based TCOs have a relatively high refractive index, ranging from 1.9 to 2.1 in the visible light spectrum, which enhances internal light absorption in semiconductor materials. In CIGS solar cell configurations, a degenerately doped metal oxide layer is typically deposited via sputtering on top of the device, serving as a transparent conductive front layer. The selection of material and layer thickness involves balancing optimal transparency with lateral conductivity, with AZO commonly used at a thickness of about 300 nm. Lateral conductivity can be further enhanced by adding a metal grid of alternating Ni/Al/Ni layers on top of the TCO [38]. Fig. 4 shows how variations in AZO thickness impact cell parameters. The short-circuit current density decreases as the window layer thickness increases, as shown in Fig. 4(a). This occurs because, with greater window thickness, fewer incident photons are able to penetrate through to the absorber layer, leading to reduced electron-hole pair generation. Consequently, the reduction in photon injections resulted in a lower J_{sc} value. For the CIGS cell, the optimal window layer thickness primarily focuses on optical optimization, as the lateral conductivity of the unwired TCO is less critical in a monolithic tandem design as bottom cell. Thus, the emphasis is on maximizing light transmission to the underlying layers rather than enhancing lateral conductivity, which has minimal impact on the overall performance of the tandem structure. Intrinsic ZnO serves an important role as a buffer layer in CIGS devices, positioned between Al–ZnO and CdS. It helps reduce shunt paths (or pinholes) between the back and front contacts. With a wide bandgap of

Table 1
Performance parameters of the investigated model.

PV Devices	J_{sc} (mA/cm^2)	V_{oc} (mV)	FF (%)	η (%)	Reference
Thin-Film CIGS (1.137 eV)	37.8	741	80.6	22.6	[1]
Thin-Film CIGS (1.13 eV)	38.5	746	79.7	22.92	[2]
Thin-Film CIGS (1.08 eV)	39.6	734	80.4	23.35	[3]
Thin-Film ACIGS (Reference cell)	38.3 (38.5)	767 (763)	80.5 (80.8)	23.64 (23.8)	[4]
Thin-Film ACIGS (Calibrated cell)	38.25	763.24	80.82	23.60	This work
Thin-Film ACIGS (Calibrated cell, Improved)	38.39	766	80.59	23.70	This work
Thin-Film ACIGS (Fixed Bandgap: 1.13 eV)	36.08	705.44	82.44	20.98	This work

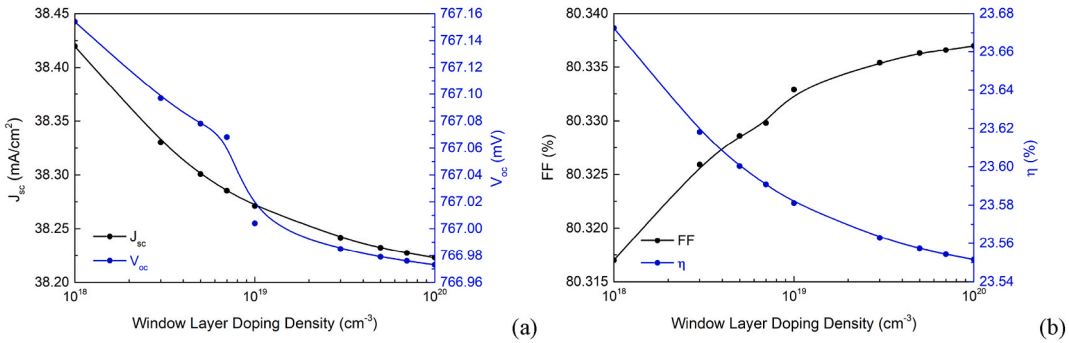

Fig. 2. Impact of window layer doping density on cell performance.

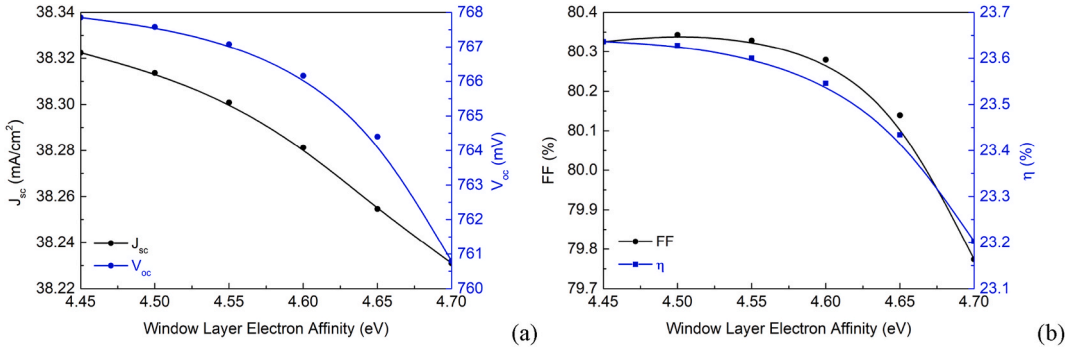

Fig. 3. Impact of window layer electron affinity on cell performance.

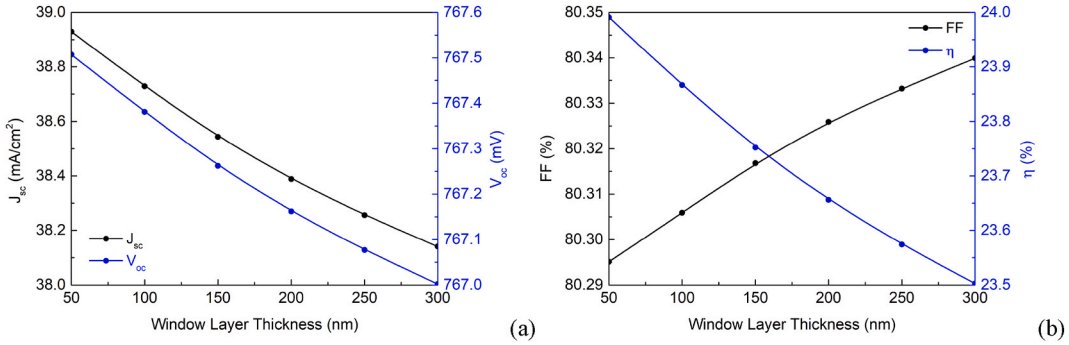

Fig. 4. Impact of window layer thickness on cell performance.

approximately 3.3 eV, intrinsic ZnO effectively transmits sunlight to the underlying CIGS layer, thereby enhancing light absorption and improving overall solar cell performance.

The doping level and synthesis method significantly influence the properties of aluminum-doped zinc oxide (AZO), enabling its customization for specific technological applications. According to the literature [39], introducing aluminum (Al) into ZnO increases the material's defectivity. Al doping alters the original hexagonal structure of ZnO by reducing its crystal symmetry and introducing various defects, such as vacancies and substitutional defects. These changes can lead to deviations in Zn–O stoichiometry, affecting the electrical, optical, and mechanical properties of the material, with defects playing a crucial role in performance for specific applications.

Janotti and Van De Walle identified several types of native defects in ZnO, classifying them into six categories [28]. These include oxygen vacancies (V_O) and zinc vacancies (V_{Zn}), as well as oxygen interstitials (O_i), zinc interstitials (Zn), oxygen antisites (O_{Zn}), and zinc antisites (ZnO) [28,40,41]. Typically, the concentration of defects (c) can be described as a function of formation energy in thermodynamic equilibrium within a solid, represented by the following equation:

$$c = N_{sites}\, exp\left(\frac{E^f}{k_B T}\right) \tag{3}$$

where N_{sites} represents the number of sites encompassing various configurations per unit volume of the defect, while E_f denotes the formation energy [28]. For this reason, we investigated the impact of defect density on cell efficiency by varying the defect cross-sectional areas (see Fig. 5). For simplicity, the defect type was assumed to be electrically neutral, with an energy level positioned at 0.5 eV within the 3.3 eV bandgap. This level represents a deep-level defect state typically associated with non-radiative recombination centers, contributing to recombination losses (see supplementary material, Table S1). Only minor variations in cell performance were observed when increasing the defect density from 10^{14} to 10^{17} cm^{-3}. This suggests that the window layer's influence on the overall device performance is predominantly optical rather than electrical in nature.

3.2. Buffer layer trade-offs

Cadmium sulfide ($Cd^{2+}S^{2-}$, CdS), a II-VI compound semiconductor, is significant due to its band gap of 2.4 eV. N-type semiconducting thin films are commonly used as buffer layers in CdTe and $CuIn_{1-x}Ga_xSe_2$ (CIGS)-based solar cells. These films can be deposited using various techniques, including vacuum evaporation [42], spray pyrolysis [43], electrodeposition [44,45], sputtering [46], and chemical bath deposition (CBD) [47], Form these methods, CBD is favored for its simplicity, low cost, low-temperature process, and suitability for large-area deposition. Using CBD-CdS thin films as buffer layers have been shown to achieve high efficiencies [13]. Typically, CdS is deposited by CBD in an alkaline solution containing cadmium salts, thiourea, and ammonia [48]. To enhance crystal quality, post-annealing or using an oscillating device during deposition can be effective [49]. Alternatively, switching from an alkaline to an acidic solution has shown promise for improving film quality [50]. The impact of different cadmium salts on the acidic CBD process has been studied systematically, showing that films with larger bandgaps and improved qualities can be produced at room temperature [51].

CdS remains the preferred material for most applications due to practical advantages, such as easy preparation under atmospheric conditions at room temperature using solution-based processes, and its stable performance [52]. Although its absorption range is limited to a portion of the visible spectrum due to its relatively large bandgap (~2.5 eV), CdS is robust and easy to handle, making it a versatile inorganic photosensitizer for various applications [53]. Despite its drawbacks, including a narrow sensitizing range and the toxic nature of cadmium, CdS has not yet been replaced by any other semiconductor material in terms of ease of preparation and broad applicability. It is likely to remain a key material until a superior alternative is discovered [52].

The wide bandgap of CdS allows efficient transmission of visible light to the CIGS absorber layer while reducing charge carrier

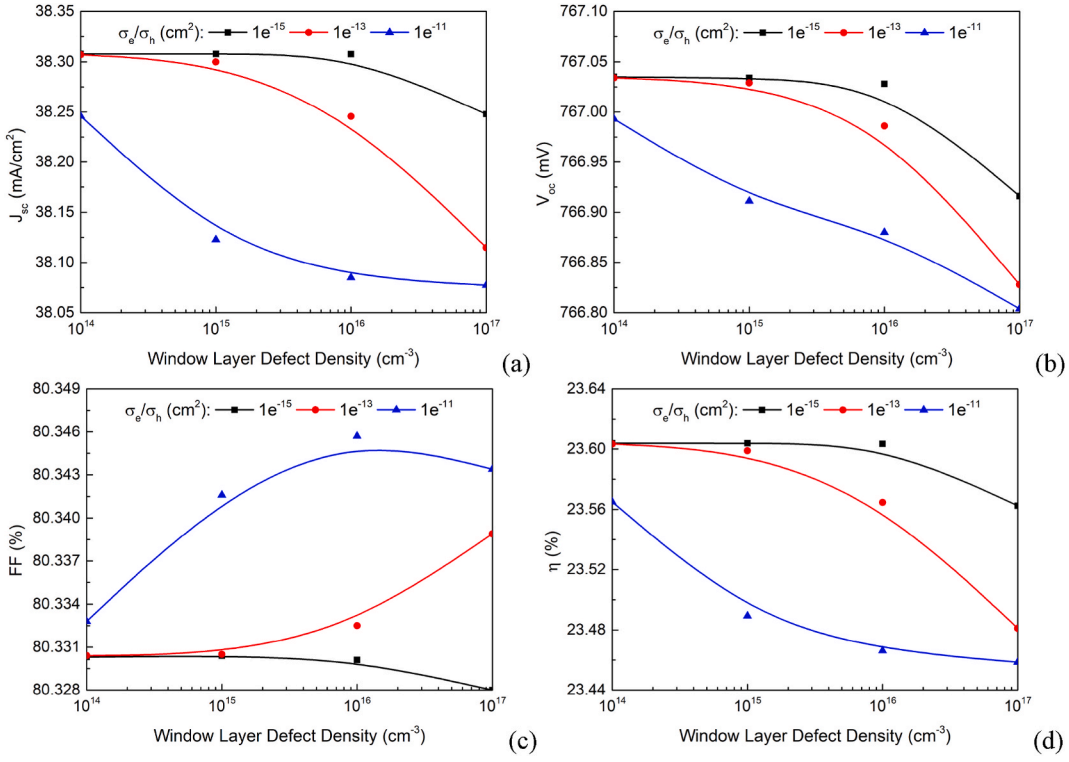

Fig. 5. Impact of defect density in the window layer with different capture cross-section for electrons (σ_e)/holes (σ_h) on cell performance.

recombination. This also minimizes surface recombination, enhancing overall cell efficiency. CdS forms a p-n junction with the CIGS absorber, which is critical for separating light-generated charge carriers and producing electrical current [52]. Typically, a 30–80 nm CdS buffer layer is applied after CIGS deposition on Mo, where it protects the CIGS during sputtering and acts as an electron-selective layer [54]. The Jan Keller group applied a standard RbF post-deposition treatment (PDT), reducing the CdS buffer thickness to 25 nm [4]. Light soaking has been shown to further optimize efficiency [4]. Although alternative materials like Zn(O,S) offer a higher bandgap, they generally result in lower efficiencies [54].

It has been shown that the CdS layer can dissipate during annealing of CdS/kesterite at high temperatures due to the diffusion of Cd and S into the kesterite, rendering the CdS ineffective as a hole barrier [55]. Consequently, an additional AZO layer is required to act as a hole-blocking layer and prevent hole injection into the front electrode [56]. Before TCO deposition, a thin resistive layer (~30 nm) is added to prevent shunting [4,57]. Intrinsic ZnO (i-ZnO) is typically used with CdS, while ZnMgO is preferred with Zn(O,S) [38].

In this work, the E_g and χ_{ACIGS} of the second top half absorber layer were fixed at 1.24 eV and 4.5 eV, respectively [4]. The χ_{CdS} and the interface defect density (D_{it}) at the ACIGS/CdS interface varied simultaneously, with values ranging from 4.0 to 4.7 eV for electron affinity, and from 10^{10} to 10^{12} cm^{-2} for defect density. As a result, the conduction band offset (CBO) between CdS buffer layer (n-type, $\chi_{CdS} = 4.2$ eV) and ACIGS absorber layer (p-type, $\chi_{ACIGS} = 4.5$ eV) can be calculated according to equation given below [58]:

$$\Delta E_c = \chi_{ACIGS} - \chi_{CdS} \tag{4}$$

The CBO sign convention is defined as follows: a positive CBO ($\chi_{ACIGS} > \chi_{CdS}$), also known as a "spike-like" CBO, requires photogenerated electrons to expend kinetic energy to overcome an energy barrier at the CdS/ACIGS heterojunction. Conversely, a negative CBO ($\chi_{ACIGS} < \chi_{CdS}$), referred to as a "cliff-like" CBO, allows photogenerated electrons to gain kinetic energy at this interface. This variation in parameters has facilitated the mapping of diverse performance characteristics across different absorber materials, which are currently being experimentally tested at the lab scale. Fig. 6 illustrates the effect of electron affinity of the CdS buffer layer with different interface defect densities on cell performance. Lowering the electron affinity in the buffer layer can create a larger conduction band offset at the absorber interface, forming an energy barrier that photogenerated electrons must overcome. This increases recombination losses and reduces charge collection efficiency, ultimately lowering the fill factor. When the electron affinity of the buffer layer becomes close to or exceeds that of the absorber, it often leads to a decrease in V_{oc}, indicating higher recombination losses within the cell. This means fewer electron-hole pairs are successfully separated and collected at the electrodes, reducing efficiency. The quality of the ACIGS/CdS interface is critical for achieving high-efficiency ACIGS solar cells. Poor interface quality (defect densities around 10^{12} cm^{-2}) can cause significant recombination, reducing V_{oc} and overall efficiency. Therefore, the deposition method and buffer layer properties must be optimized to minimize interface defects.

To optimize minority carrier transport, the CdS layer should be as thin as possible to reduce series resistance and absorption loss

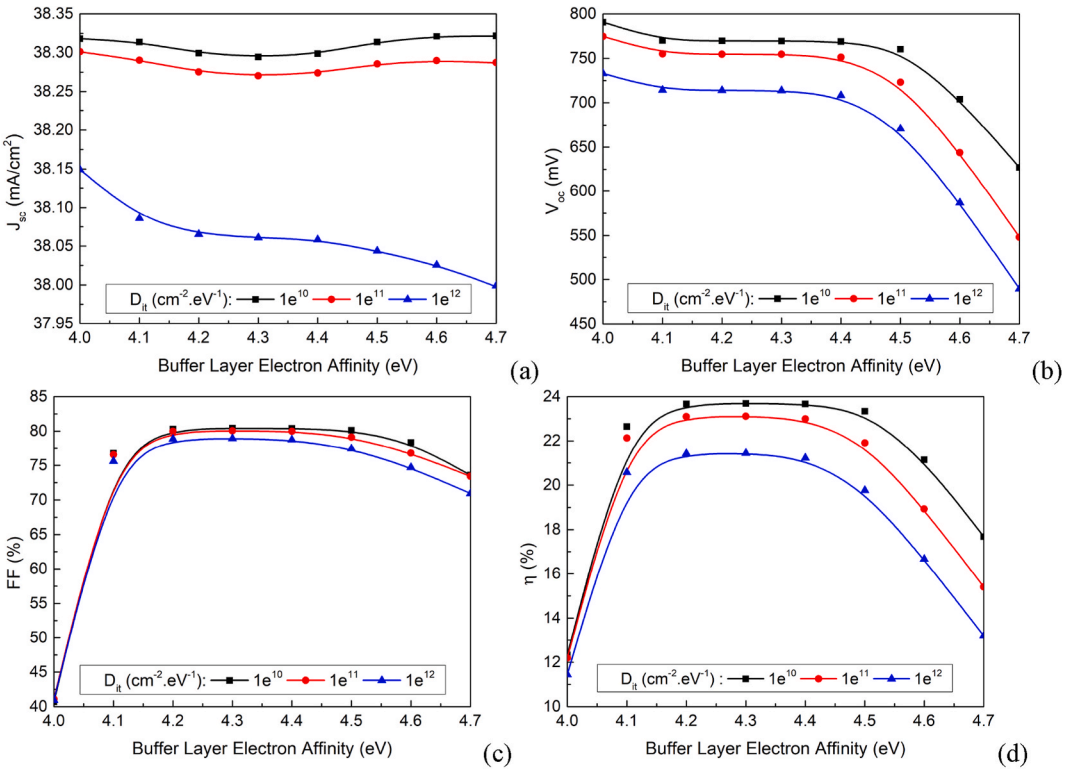

Fig. 6. Impact of buffer layer electron affinity with different interface defect density at CdS/ACIGS interface on cell performance.

[59]. A thicker layer could diminish the Schottky barrier's efficiency. To enhance CdS conductivity, a process known as doping is applied, where intentional impurities, either acceptor or donor atoms, are introduced into the semiconductor's crystal lattice [60]. Doping can be chemically achieved during growth by adding controlled amounts of a dopant salt solution to the reaction, without damaging the lattice structure [61]. Although there are studies on doping CdS with various elements such as Silver (Ag), Copper (Cu), Chlorine (Cl), Indium (In), Aluminum (Al) and others, most focus on nanoparticles, with few examining thin films, highlighting the need for further exploration. Chandramohan et al. (2009) showed that cobalt (Co) doping alters CdS's optical band gap by introducing localized energy states at the band edges [62]. Similarly, Sebastian (1993) found that doping with copper (Cu) during chemical bath deposition (CBD) reduced the bandgap to approximately 2.0 eV [63]. Portillo-Moreno et al. (2006) also reported an increase in CdS resistivity with Cu doping [64]. Sánchez et al. (2014) demonstrated that Cu-doped CdS, when used as the window layer in CZTS solar cells, improved voltage, addressing the voltage deficit issue in such devices [65]. Additionally, Challa et al. (2012) observed that boron (B) doping reduced dark resistivity and enhanced the photosensitivity of CdS thin films [66]. Hani Khallaf investigated the effects of in situ doping of CdS using aluminum (Al), gallium (Ga), boron (B), and indium (In) via the CBD method and found it effective [67]. In all cases, increasing the [Al, Ga, B, In]/[Cd] ratio in the solution significantly reduced the bandgap of doped CdS films [68]. Alhammadi et al. (2018) explored Ga-doped CdS in CIGS solar cells and found that photocurrent density improved, and cell efficiency increased slightly from 9.69 % to 10.37 % [69]. The donor concentration is adjusted based on the values presented in Fig. 9. As a result, the electrical resistivity of the CdS buffer layer varies according to Equation (5), as detailed below [70]:

$$\rho = \frac{1}{q\mu_n N_D} \tag{5}$$

where ρ represents resistivity, q is the charge of the electron, and μ_n and N_D denote the electron mobility and donor concentration of the CdS buffer layer, respectively.

In this study, we investigate how doping and buffer layer thickness affect the cell performance. Initially, we analyzed the impact of CdS buffer layer doping on cell performance, using a 25 nm-thick layer and varying the dopant concentration (Fig. 7). The results show that as the dopant concentration increases, cell performance improves up to a certain level, stabilizing beyond a concentration of $N_D = 10^{18}$ cm^{-3}, with minimal further improvements. This indicates that doping significantly affects solar cell efficiency, and $N_D = 10^{18}$ cm^{-3} is identified as the optimal concentration for maximizing performance.

We also investigated the impact of CdS buffer layer thickness on solar cell efficiency (Fig. 8), with thicknesses varying from 10 to 50 nm. As the thickness increased, the short-circuit current density remained relatively stable, showing only slight degradation. The open-circuit voltage increases with greater buffer layer thickness, attributed to enhanced photon absorption beyond the hole diffusion length, which lowers the recombination rate. However, V_{oc} is also influenced by the carrier concentration in the buffer layer, which limits further increases; thus, V_{oc} begins to decline after reaching a certain thickness (beyond 35 nm). In heavily doped CdS, the carrier concentration is so elevated that the recombination rate does not significantly impact V_{oc}, resulting in a consistent decrease for this structure, as illustrated in Fig. 8. The optimal thickness was found to be within the 20–40 nm range. During the deposition process, this thickness is critical, as excessively thick layers can hinder the number of photons reaching the absorb layer, ultimately affecting the overall performance of the device.

In the previous section, it was found that adding dopants improves the conductivity of CdS. Additionally, the electrical properties of CdS can be altered through doping, with reports indicating successful doping using elements such as Mn, Cu, Ni, Co, Ga, B, and Ag [66, 71–76]. Doping has been shown to reduce the energy gap of CdS films by introducing trap states and impurities within the energy gap region. During the preparation of thin films, various defects may form, including voids, interstitials, dislocations, and strains. These defects play a crucial role in altering optical absorption by acting as trap centers. Consequently, the reduction in the energy gap is primarily attributed to defect band tailing due to the creation of localized energy states along the band edges. It has been observed that undoped CdS films exhibit higher absorbance compared to doped films [77].

The decrease in absorbance is likely due to defect states resulting from lattice imperfections caused by different dopant concentrations [77]. The optical energy gap (E_{opt}) and optical absorption coefficient (α) in a direct transition semiconductor are related as

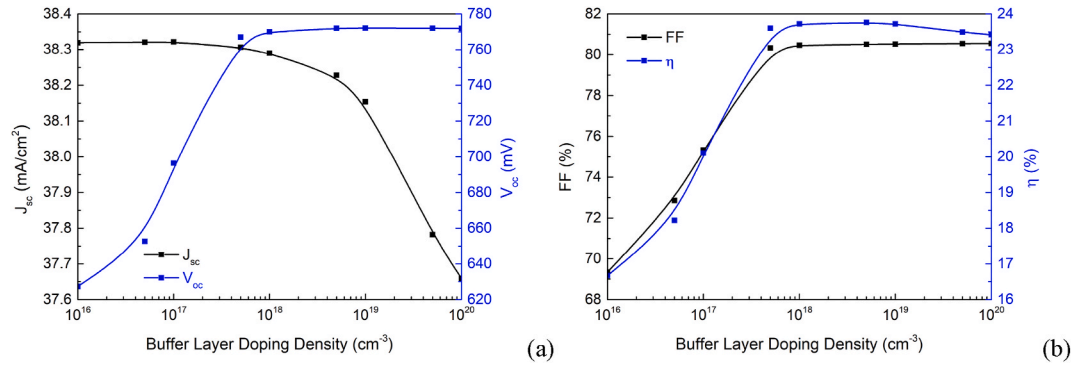

Fig. 7. Impact of buffer layer doping density on cell performance.

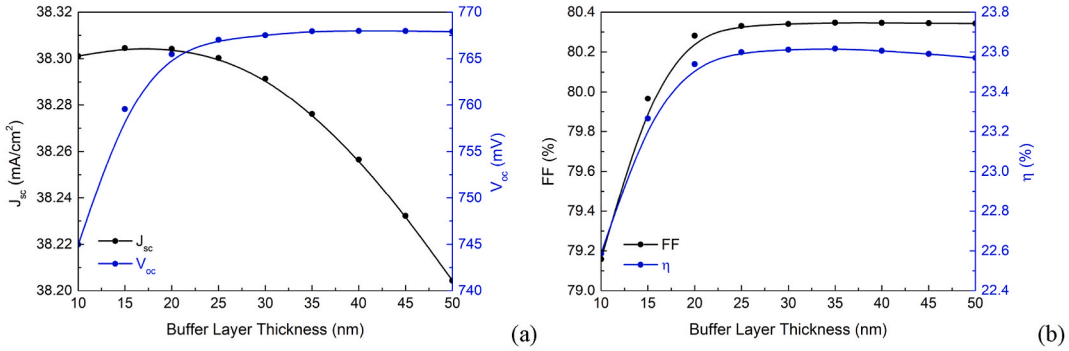

Fig. 8. Impact of buffer thickness on cell performance.

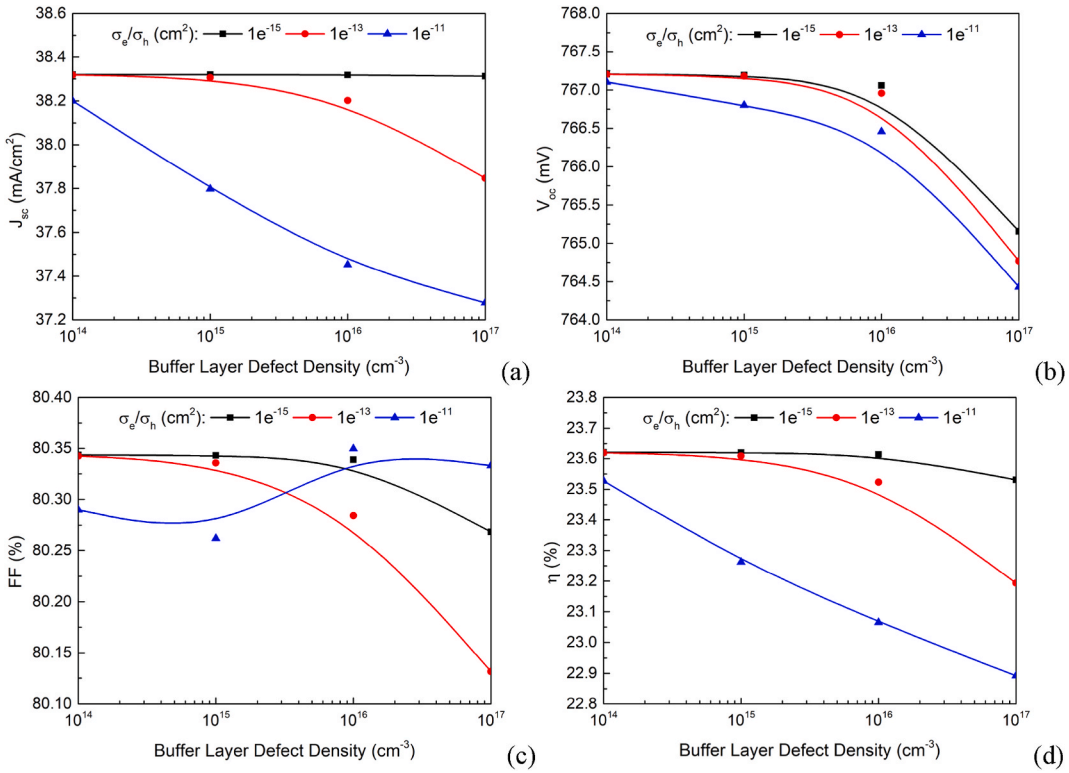

Fig. 9. Impact of defect density in the buffer layer with different capture cross-section for electrons (σ_e)/holes (σ_h) on cell performance.

follows:

$$\alpha h\nu = B\left(h\nu - E_g\right)^{\frac{1}{2}} \tag{6}$$

where B is a material-dependent constant, E_g represents the direct energy gap, hv is the photon energy, and α is the absorption coefficient. For direct energy gap materials, a value of 0.5 is typically assumed. Based on this, we explored the effect of defect density in CdS layer on overall cell performance, considering various cross-sectional defect areas, as shown in Fig. 9. To enhance the concept of doping in CdS thin films, a fundamental understanding of how doping impacts the optical, morphological, structural, and electrical properties is essential. This knowledge would clarify the mechanisms influencing CdS thin film formation [59].

3.3. Absorber layer ACIGS

Chalcopyrite ($CuInSe_2$), a semiconductor composed of Copper (Cu), Indium (In), and Selenium (Se), is recognized for its brassy-yellow appearance and tetragonal crystal structure [78,79]. Since Han et al. synthesized chalcopyrite $CuInSe_2$ in 1953, copper

indium gallium selenide (CIGS) has increasingly been utilized in solar cells due to its favorable properties, like a high absorption coefficient and an optimal band gap for converting sunlight into electricity [4,78,79]. The bandgap of $Cu(In_{1-x}Ga_x)Se_2$ is typically tuned by modifying the [Ga]/([Ga] + [In]) ratio (GGI), which makes it an ideal candidate for single junction as well as tandem application [4,80–82]. A transition from $CuInSe_2$ (CIS, $E_g \approx 1.04$ eV) to $CuGaSe_2$ (CGS, $E_g \approx 1.68$ eV) would shrink the lattice of the crystal [83]. As a result, the bandgap would vary from 1.04 eV for CIS to 1.68 eV for pure CGS [84]. Intermediate bandgap values can be reached by tuning the GGI between 0 and 1. For high bandgap applications, Se can be also substituted by sulfur [38]. In addition to optimizing the absorption of light to a certain range of wavelength, it is often beneficial to tune the GGI across an absorbing layer to form a graded bandgap CIGS layer. GGI would be preferably lower at the bulk and higher at the anode and cathode sides, a 'notch' (sometimes also 'V-shaped') GGI profile, to minimize the recombination at the interfaces [38].

CIGS films for thin-film photovoltaic technology can be fabricated on both rigid and flexible substrates using a range of vacuum and non-vacuum techniques. Among the vacuum-based methods, co-evaporation [13], physical vapor deposition (PVD) [14], pulsed laser deposition (PLD) [15], chemical vapor deposition (CVD) [16], metal-organic chemical vapor deposition (MOCVD) [17], electron beam deposition (EBD) [18], molecular beam epitaxy (MBE) [19], and sputtering [20,21] are frequently employed.

Vacuum deposition techniques differ in how the materials are applied, either through a multi-stage process where each element is deposited sequentially [13], or by direct deposition, in which the CIGS and other layers are deposited in a single step [15,85]. In co-evaporation processes, such as PVD, MOCVD, and MBE, the CIGS layer is typically grown in multiple stages, with a constant Se flux to achieve a graded composition and a Cu-poor surface. This approach, involving the separate deposition of In and Ga from Cu and controlled Cu levels during initial and final stages, is crucial for forming a graded bandgap and reducing recombination at the Cu-poor interface, which ultimately enhances solar cell efficiency [38].

Single-step processes, such as PLD and sputtering, offer advantages in terms of time and cost efficiency. PLD, while limited to small-area production, is suitable for laboratory-scale applications [85], whereas sputtering enables large-area CIGS deposition, making it ideal for industrial-scale manufacturing [20,21]. Despite the high-quality samples that can be produced via vacuum techniques, these methods have notable limitations, such as high costs, time-intensive processes, and challenges in achieving uniformity over large areas due to cosine flux distribution, which can lead to abrupt changes in film composition and reduced Se incorporation [38,86]. To improve efficiency, vacuum methods are most effective when used in a continuous full-stack deposition system without breaking the vacuum [14]. However, almost all deposition techniques require a post-selenization process to optimize the CIGS composition. This often necessitates breaking the vacuum for additional selenization steps, such as rapid thermal processing or reactive annealing, to achieve the desired material properties [87].

In our study of the thin-film ACIGS absorber layer, a 'hockey stick'-like gallium gradient index (GGI) profile was implemented for the 2 μm thickness, featuring a constant Ga content in the upper half of the absorber and a significantly increased concentration near the back contact [4]. The band gap value of the absorber layer at the front was fixed at 1.24 eV, while the electron affinity varied from 4.0 to 4.5 eV. Additionally, a neutral deep defect located around $\sim E_g/2$ was introduced in the bulk of the ACIGS layer. As explained in the buffer section, the band alignment at the buffer/absorber interface in a ACIGS solar cell strongly affects the performance [57].

Fig. 10 illustrates the effect of electron affinity of the ACIGS absorber layer on cell performance. Fig. 11 illustrates the effect of interface trap density at CdS/ACIGS interface with different cross-section on cell performance. Increasing the electron affinity in the ACIGS absorber layer can create a larger conduction band offset at the CdS/ACIGS interface, forming an energy barrier that photo-generated electrons must overcome. This increases recombination losses and reduces charge collection efficiency, ultimately lowering the fill factor, as can been seen when the value is above 4.4 eV. When the electron affinity of the absorber layer becomes lower than or close to that of the CdS, it often leads to a decrease in J_{sc} and V_{oc}, indicating higher recombination losses within the cell. This means fewer electron-hole pairs are successfully separated and collected at the electrodes, reducing efficiency. As has been explained in the previous section (Buffer section), the quality of the ACIGS/CdS interface is critical for achieving high-efficiency ACIGS solar cells. An optimum value can be extracted for a value of 4.4 eV and 4.2 eV for ACIGS and CdS, respectively. It has been found that the band alignment can be affected by deposition temperature of buffer layer [88,89]. It is important to determine whether the changes in E_g at different deposition temperatures are primarily associated with variations in the conduction band energy rather than in the valence band energy [88,89]. Fig. 12(a) illustrates the band diagrams at short circuit conditions for different CBO configurations. As shown in

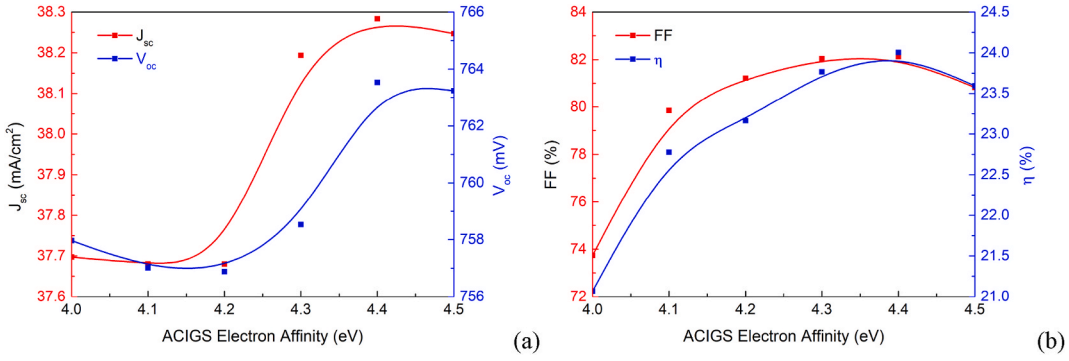

Fig. 10. Impact of absorber electron affinity on cell performance.

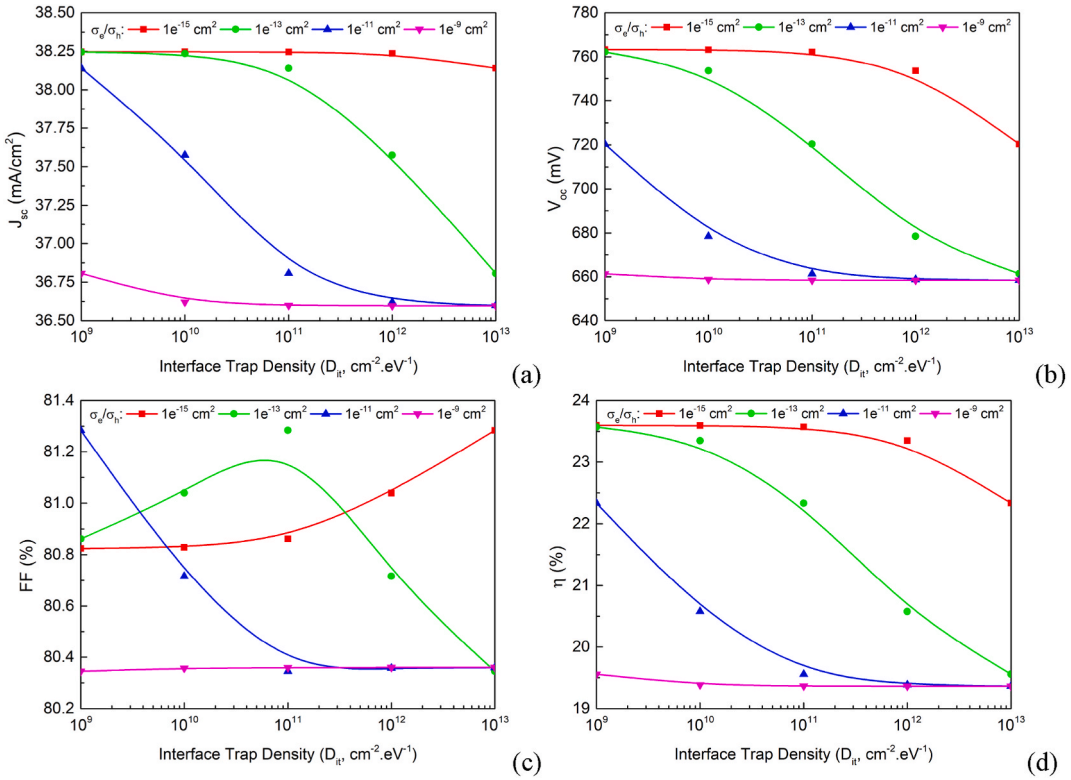

Fig. 11. Impact of interface trap density at CdS/ACIGS interface on cell performance.

Fig. 12, the difference between the CdS and CIGS semiconductors bandgaps creates conduction and valence band discontinuities. Thus, $E_g \leq 2.2$ eV results in a negative (cliff) CBO to the absorber, while $E_g \geq 2.4$ eV produces in a positive (spike) CBO. The optimum values have been taken into consideration in order to achieve high device efficiency, see Fig. 12(b) at AM 1.5 spectrum illumination. The key material parameters used to model the CdS/ACIGS solar cells for various transport mechanisms are summarized in Table 2. In the thermionic mechanism, the Richardson constants are typically assigned default values based on the effective density of states in both the conduction and valence bands.

3.3.1. Influence of doping and thickness of absorber layer on cell efficiency

Cell performance can be significantly affected by the deposition techniques, which influence growth, crystallization, grain size, bulk defect, and interface defect, thereby impacting on photogenerated charge carriers' collection. The device discussed in this section is the same as the one reported by Jan Keller et al. [4]. The ACIGS absorber, with a thickness of 2 μm, was deposited onto a 290 nm thick Mo metal back contact using a 3-stage co-evaporation process [7]. This method effectively creates an ACIGS layer with either

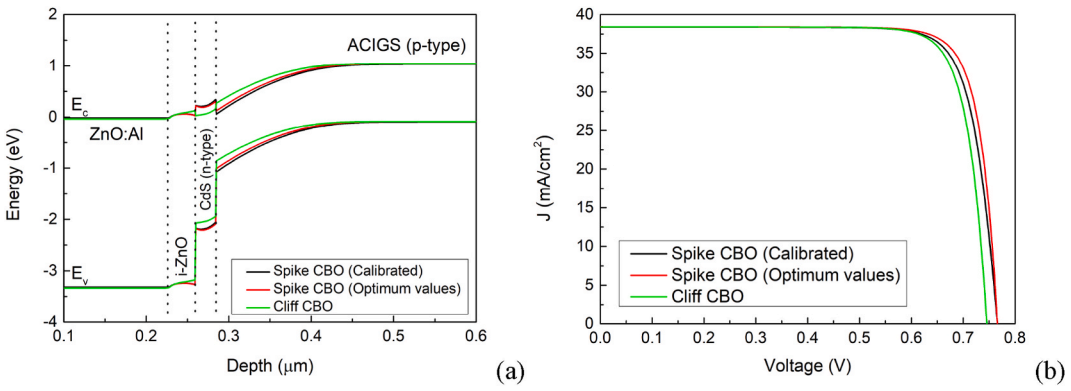

Fig. 12. (a) Band diagram for a simulated ACIGS device with CdS bandgap of 2.4 eV and 2.1 eV at short-circuit conditions (b) J–V curves at spike and cliff CBO configuration at AM 1.5 spectrum illumination.

Table 2
Performance parameters of the models investigated at different transport mechanisms and CBO configurations.

Transport mechanism at CdS/ACIGS interface	PV Devices	J_{sc} (mA/cm^2)	V_{oc} (mV)	FF (%)	η (%)
Diffusion (SRV = 1 × 10^2 cm/s)	Reference Cell	38.39	766.01	80.59	23.70
	Spike CBO (Optimum): χ_{ACIGS} = 4.4 eV (Graded banggap) χ_{CdS} = 4.2 eV (Eg = 2.4 eV)	38.42	765.81	82.18	24.18
	Cliff CBO: χ_{ACIGS} = 4.4 eV (Graded banggap) χ_{CdS} = 4.5 eV (Eg = 2.1 eV)	38.41	745.80	81.61	23.38
Thermionic emission and Tunnel	Spike CBO (Default)	38.38	752.49	80.36	23.21

single or double-graded Ga distribution, influencing the conduction band throughout the depth of the ACIGS film [8]. In the reference cell, the x value was graded in the first stage (the lower half of the absorber) and kept constant in the second stage (the upper half of the absorber), resulting in a 'hockey stick'-like GGI profile. To simplify the deposition process, we modeled a 2-stage process. In the first stage, In-Ga-Se is co-evaporated onto heated Mo with a higher Ga rate compared to In, targeting a depth of ≥1000 nm. In the second stage, In-Ga-Se is co-evaporated again with a fixed Ga rate that is lower than that of In, achieving a bandgap around 1.13 eV for the ACIGS absorber. A schematic diagram illustrating the bandgap profile of the bottom ACIGS subcell is provided in the supplementary material (Fig. S1), showing a single-graded bandgap starting from 1 μm below the front surface of the ACIGS film. The grading profile shape in the CIGS absorber layer results from the diffusion of Ga and In. The value of x_1 is increased to 0.76 toward the rear contact to align with the fabricated model and achieve a more linear grading profile. This adjustment helps to accelerate electrons towards the ACIGS/CdS surface due to the electric field, thereby reducing rear recombination. Although many studies have addressed the improvement of composition and thickness uniformity in the ACIGS layer, there has been little research on the quantitative analysis of how non-uniformity impacts large-area CIGS manufacturing lines [90]. It has been observed that controlling the thickness of CIGS films is not solely dependent on reducing the deposition time of the Cu–In-Ga layers, without considering adjustments to the composition and deposition parameters of the thin film [90]. A two-step process, involving the electrodeposition of Cu–In-Ga followed by annealing in a pure Se atmosphere, revealed that simply decreasing the deposition time does not sufficiently reduce the thickness of the precursor layers [90]. Comprehensive adjustments to both the composition and deposition conditions are necessary. Furthermore, despite a reduction in thickness and consequently a decrease in short-circuit current density, the open-circuit voltage of ultrathin CIGS solar cells fabricated through electrodeposition can be enhanced by increasing the Ga content within the absorbers [90].

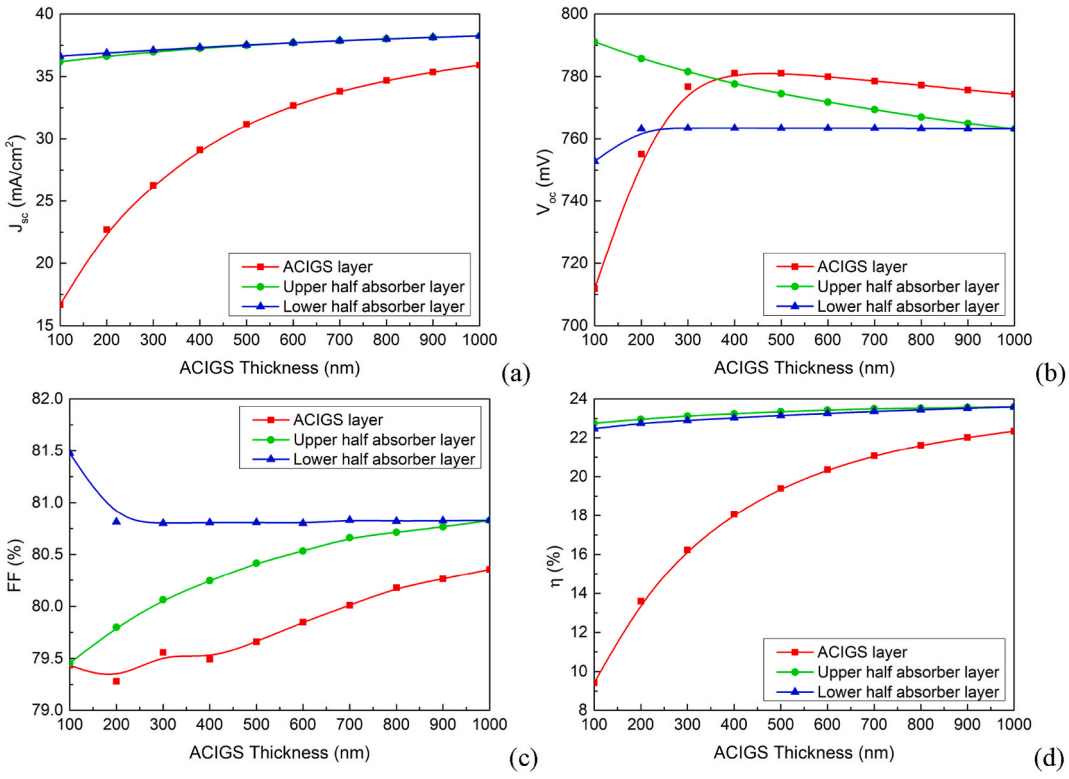

Fig. 13. Impact of absorber thickness on cell performance.

In this section, the thickness and dopant concentration of the absorber have been varied for whole layer (ACIGS layer) and for two different stages (upper and lower half absorber layer), it is a very good experiment to analyze the impact of these two quantities on cell performance (See Figs. 13 and 14). The thicknesses and dopant concentration were varying from 100 to 1000 nm and from 10^{14} to 10^{18} cm^{-3}, respectively. For example, while varying for half layers, one was kept fixed at 1000 nm and 10^{16} cm^{-3}. Very low J_{sc} is observed with thin layers (Red color), these effects can arise from the following mechanisms: (i) optical loss due to the insufficient absorption capacity of the ACIGS absorber layer, (ii) recombination at the front CdS/ACIGS interface, and (iii) recombination within the space charge region (SCR). The SCR significantly influences carrier collection, particularly when the ACIGS absorber thickness approaches the widths of the SCR. Generally, the electric field within the SCR facilitates efficient collection of photogenerated carriers, as well as the charge reaching the SCR through diffusion from the neutral region (i.e., outside the SCR) of the ACIGS. Increasing the ACIGS absorber layer will generate more carriers, enhancing J_{ACIGS}. V_{oc} generally tends to increase while increasing both absorber thicknesses till a certain limit, except for upper layer. As for FF, it depends on internal series resistance which is different compared to the standalone device. From these three samples, an optimum value can be extracted for η while varying the thicknesses. The optimal depth could be extracted for upper half, being approximately 100 nm below the front surface. V_{oc} decreases by 30 mV with an increase in the depth of the second region from 100 nm to 1000 nm. The fill factor remains above 78 % among all samples. Increasing the depth beyond the charge region improves FF due to increased shunt resistance (R_{sh}), as shown in Fig. 13(c). This improvement helps to prevent leakage current and facilitate carrier transport at the junction. However, for multi-stage deposition process, the upper half region has a strong effect on cell efficiency across all samples when it is below 500 nm thick.

Intrinsic p-type doping of CIGS can be achieved by tuning the [Cu]/([Ga] + [In]) ratio (CGI). Cu deficiency induces the formation of V_{-Cu} states, which can act as acceptor states and have a low formation energy. They can form neutral pairs with (In_{Cu}^{2+},Ga_{Cu}^{2+}), and in general CIGS has a certain defect tolerance as off stoichiometry compounds can be formed [91]. CIGS absorber layers can also be doped by alkali incorporation [92]. Na generally diffuses from the soda-lime glass substrate to the CIGS layer, and other species such as K and Rb can be implemented through post-deposition treatments. These species passivate the CIGS absorber surface as well as its grain boundaries and increase the p-type carrier concentration in the layer. This phenomenon results in a lower E_F, and ultimately in an increase in V_{oc} and FF for completed cells. It has been reported that the improvements in the device due to Na doping are linked to enhanced p-type conductivity and defect passivation [93], though the specific underlying mechanisms remain a topic of debate. Some suggest that Na catalyzes the oxygenation of Se vacancies [94], forms $Na_{(In,Ga)}$ acceptors [95], eliminates $(In,Ga)_{Cu}$ donors [96], or increases the concentration of Cu vacancies (V_{Cu}) due to the differential solubility of NaCu during CIGS growth and cooling [97]. Each of these proposed mechanisms has its strengths and weaknesses, but none fully account for all the experimental evidence or withstand theoretical scrutiny. Furthermore, the effects of Na doping in CIGS extend beyond electronic properties; in addition to hindering

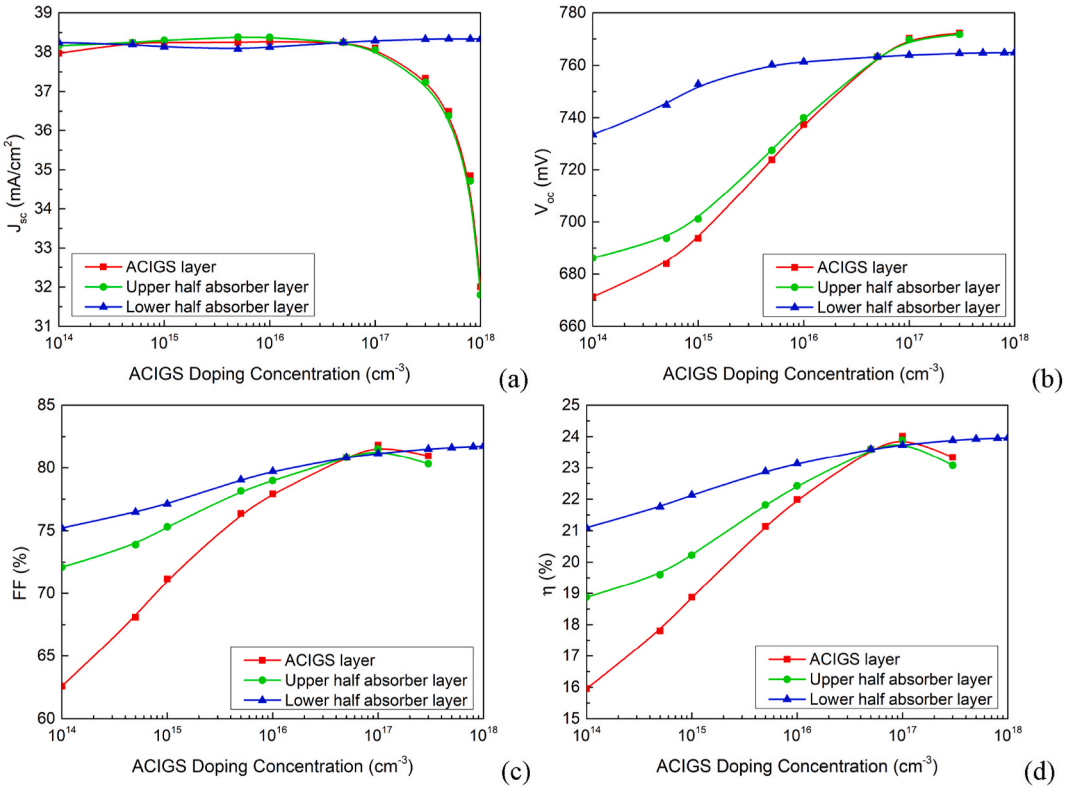

Fig. 14. Impact of absorber doping concentration on cell performance.

atomic diffusion [98], Na also influences grain growth and texture [99,100]. Among the various substrate types used, soda lime glass has been shown to be the most suitable option, as it better matches the thermal expansion coefficient of the molybdenum back contact [101]. Additionally, sodium diffusion from the SLG (through the Mo layer) into the CIGS absorber layer significantly enhances overall cell performance. This effect is primarily associated with the passivation of grain boundary defects, an increase in carrier density, and changes in crystal orientation resulting from Na incorporation in the CIGS layer [101]. Colombara et al. demonstrated that background sodium contamination from routine annealings in the presence of SLG or Na salts serves as a parallel doping source and significantly impacts the performance of CIGS devices [96].

For this reason, it is important to demonstrate how the dopant concentration of the whole layer (ACIGS layer) and at two different stages (upper and lower half absorber layer) of CIGS absorbers can affect device performance. Fig. 14 illustrates the impact of absorber doping concentration on cell performance. From Fig. 14 (a) it is apparent as slight variations in J_{sc} when the concentration level is below $N_A = 10^{17}$ cm^{-3}. As was reported previously, the J_{sc} follows same trend as grain side variation [101]. Increased p-type doping led to an increase in V_{oc} and FF of this device as shown in Fig. 14(b and c). This means the bulk dopant density influences bulk resistivity (related to FF) and bulk lifetime (related to V_{oc}). An increase in dopant concentration uniformly across the entire ACIGS layer results in improvements of approximately +15 % in V_{oc} and +30 % in FF. Furthermore, an efficiency variation of 25 % near the front side leads to greater performance enhancement compared to a 12 % improvement when the same dopant variation is applied at the rear side. This highlights the critical importance of optimizing dopant concentration near the front junction (CdS/ACIGS interface) to maximize device performance. Increasing the doping level in the absorber layer leads to enhancing cell performance due to the built-in electric field (V_{bi}) across the solar cell [102]. However, excessive dopant can increase Auger recombination and reduce carrier mobility, so finding the optimal concentration is key, as shown in our simulations. The results show that as the dopant concentration increases, cell performance improves up to a certain level, stabilizing beyond a concentration of $N_A = 10^{17}$ cm^{-3}, with minimal further improvements. This indicates that doping significantly affects solar cell efficiency Fig. 14(d), and $N_D = 10^{17}$ cm^{-3} is identified as the optimal concentration for maximizing performance.

3.3.2. *Influence of defect density and cross-section on cell efficiency*

Crystal lattice defects are critical material properties, playing a pivotal role in the performance of solar cells. These defects significantly impact the generation, separation, and recombination of electron-hole pairs within the absorber layer. Defects refer to disruptions in the periodic arrangement of atoms within the crystalline structure. A defect state is considered shallow if its energy level is close to the conduction band minimum or the valence band maximum, while deeper defect states exist farther from these band edges.

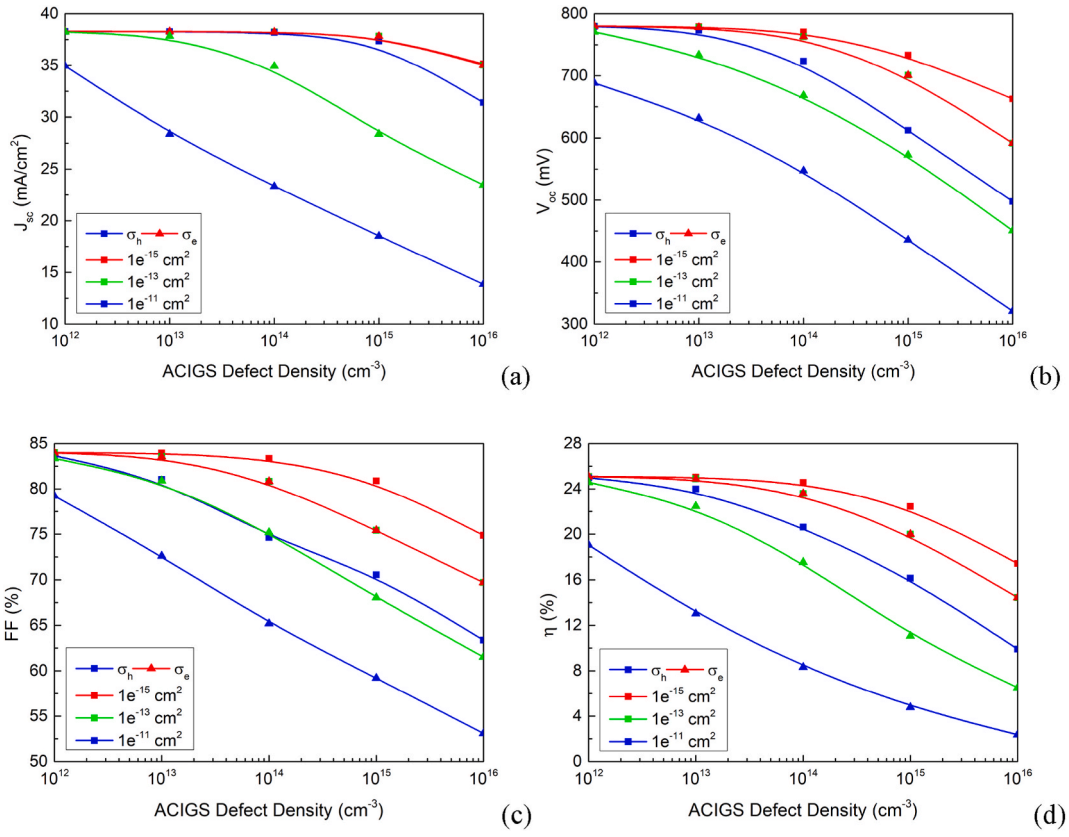

Fig. 15. Impact of absorber bulk defect density with different capture cross-section areas on cell performance.

Shallow defects typically act as dopants, introducing charge carriers into the material, whereas deep defects act as traps, capturing carriers introduced through doping [101]. Understanding and controlling these defects and impurities, which form various energy levels, is crucial for optimizing solar cell performance. Fig. 15 highlights the effect of defect density, including different capture cross-section areas for electrons and holes, on cell efficiency. The defect levels were introduced at the mid-gap of the absorber layers. It clearly demonstrates how increased defect density can degrade cell performance. These findings provide valuable insights for the thin-film photovoltaic community, underscoring the importance of managing defects during the growth process and in the introduction of impurities [101].

3.4. ACIGS solar cell optimization

In this study, we integrate recent key research insights to advance device efficiency through detailed numerical modeling. The ACIGS (Silver-doped Copper Indium Gallium Selenide) structure was optimized, resulting in significant performance improvements. A strong correlation between the simulated and experimental results for standalone solar cells validates the accuracy and reliability of our model [4,18]. To enhance photon absorption and device efficiency, magnesium fluoride (MgF_2) was employed as an anti-reflection coating (ARC) layer. Recent studies suggest further improvements by relocating the MgF_2 ARC to the outermost surface above the glass layer, thereby increasing photon capture efficiency [8]. In the reference device, a 'hockey stick'-like gallium grading (GGI) profile was implemented. From our previous work, we identified that samples with specific grading parameters $x_1 = 0.70$ (lower absorber region), $x_2 = 0.35$ (upper absorber region), and a notch position located 100–200 nm from the junction demonstrated high potential for achieving efficient ACIGS solar cell designs [103–106]. The highest reported efficiency for a standalone ACIGS cell, 25.86 %, was attained by optimizing key parameters, including: doping concentration ($N_A = 1 \times 10^{17}$ cm^{-3}), electron affinity ($\chi_{CIGS} = 4.4$ eV), gallium grading ($x_1 = 0.70$, $x_2 = 0.35$), notch depth (100–200 nm), and minimizing carrier capture cross-sections ($\sigma_{e/h} = 1 \times 10^{-14}$ cm^2) within the absorber layer. Based on our earlier findings that demonstrated an approximate 5 % increase in efficiency through double gallium grading ($x_1 = 0.70$ toward the back, $x_2 = 0.35$ toward the front), we adopted a similar strategy here to further enhance the open-circuit voltage [105]. Experimental studies have also explored bandgap grading by incorporating silver (Ag) into CIGS films to improve electrical conductivity [7,8,107]. To minimize interface recombination, an interface trap density of 1×10^{10} cm^{-2} eV^{-1} was introduced at the CdS/ACIGS interface. The degradation of CdS-buffered ACIGSe solar cells under thermal stress is largely independent of the annealing environment (air or vacuum) but strongly influenced by sodium diffusion and Cd interdiffusion. The presence of Na, particularly when diffusing from the CIGSe absorber into the CdS and TCO layers due to interactions with water and OH^- in the CdS layer, is the main cause of degradation, leading to acceptor-like defect formation, cliff-like band alignment at the CIGS/CdS interface (lowering V_{oc} and τ_e), and Cd diffusion into the absorber (promoting n-type defects) [108]. The reduced carrier lifetime (τ) can be primarily attributed to an accelerated carrier trapping process. A faster trapping rate at the interface implies a significantly higher interface trap density compared to the bulk, leading to increased non-radiative recombination [109]. Molybdenum was used as the back contact to reduce rear-side light reflection. This configuration significantly improves both short-circuit current density and V_{oc}. Additionally, the optimized model showed a 15 % reduction in computational convergence time, enhancing simulation efficiency and practical feasibility. Fig. 16 presents the J–V curves and EQE spectra of the optimized ACIGS structure compared to the reference (calibrated) cell. The optimized device achieves a high short-circuit current density of 38.48 mA/cm^2, a fill factor exceeding 84.87 %, and an open-circuit voltage of 795.35 mV. A comprehensive performance summary is provided in Table 3, benchmarking this photovoltaic (PV) cell model against recent literature [4].

3.5. Impact of temperature and light intensity on cell performance

ACIGS technology has a well-established outdoor performance record [4]. The PCE of the single-junction ACIGS devices under strander test conditions (STC, AM1.5 and T = 25 °C) were 23.60 % and 25.80 % for reference and optimized cell (200 nm Notch depth), respectively. For temperature and light intensity testing, we perform J–V measurements at different temperatures (20–90 °C) and

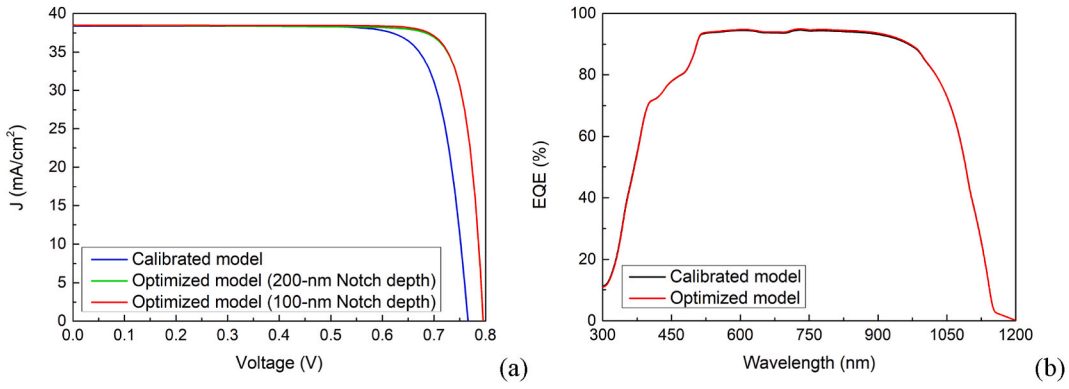

Fig. 16. J–V curves and EQEs of optimized ACIGS models in comparison with the reference model (Calibrated).

Table 3
Performance parameters of the optimized models.

PV Devices	J_{sc} (mA/cm^2)	V_{oc} (mV)	FF (%)	η (%)	Ref.
Optimized model (100 nm Notch depth)	38.48	795.35	84.87	25.98	This work
Optimized model (200 nm Notch depth)	38.47	795.18	84.53	25.86	This work
Calibrated model	38.39	766.01	80.59	23.70	This work
Fabricated ACIGS model	38.3 (38.5)	767 (763)	80.5 (80.8)	23.64 (23.8)	[4]

under different light intensities (10–120 mW/cm^2, 10–120 % light intensity). Fig. 17 illustrates the Shockley-Read-Hall (SRH) recombination rate across the ACIGS absorber under both low and high-temperature conditions. The SRH recombination mechanism, which is a dominant recombination process in the absorbers, tends to increase with temperature due to enhanced carrier trapping by defects and impurities within the cell. The figure shows as the temperature increases, there is a significant rise in the recombination rate, especially near the buffer/absorber interface and in the depletion region. This increase in SRH recombination at high temperatures can lead to reduced carrier lifetimes and ultimately lower cell efficiency. In Fig. 18(a and b), we illustrate the impact of temperature on the J–V and P–V curves under constant irradiation (100 mW/cm^2). Results indicate that the primary cause for PCE reduction with temperature is a drop in voltage, aligning with the detailed balance limit, while J_{sc} remains mostly unaffected. These curves allowed us to calculate the power temperature coefficient for the ACIGS device studied. In Supplementary Material Fig. S2, a detailed analysis of J–V characteristics for reference and optimized cells across different temperatures are presented. In Figure S2 (a), we observed that J_{sc} in ACIGS is largely stable with temperature, though ACIGS shows a substantial decrease in FF as temperature rises, as depicted in Figure S2 (c). The resulting slopes yield power temperature coefficients of $k_{th\_power} = \gamma = -0.242\ \% K^{-1}$ for reference and $-0.207\ \% K^{-1}$ for optimized ACIGS cells, consistent with values reported by literature and module manufacturers [12]. In Fig. 19(a and b), we demonstrate the effect of light intensity on J–V and P–V curves at a constant temperature of 25 °C, while Fig. 20 shows V_{oc} and FF as functions of light intensity for temperatures of 25 °C, 50 °C, and 90 °C. From data at 100 % light intensity (100 mW/cm^2), we extracted voltage temperature coefficients of $k_{th\_Voc} = \beta = -0.18\ \% K^{-1}$ and $-0.14\ \% K^{-1}$ for the reference and optimized cells, respectively. Across all tested temperatures, V_{oc} decreases logarithmically with light intensity, with an ideality factor $n = 1.53$ derived from the slope. A marked reduction in FF with temperature was observed in ACIGS, which further increases k_{th_P}, possibly due to changes in material properties like conductivity and energy alignment. For environmental protection, solar cells in modules are generally encapsulated with 3.2 mm thick glass and a 500 μm encapsulation foil. This encapsulation changes CIGS optics by increasing reflection and parasitic absorption in the UV range, which reduces J_{sc}. The numerical findings from this study are valuable for developing high-efficiency solar cells, providing critical insights into how device parameters respond under various conditions. These results enhance researchers' and engineers' understanding of underlying mechanisms, such as recombination processes, carrier transport, and material property effects on performance. Additionally, the study's findings could aid in interpreting and complementing experimental results, offering a deeper understanding of how specific design choices influence the efficiency and stability of solar cells in real-world applications. This synergy between simulation and experiment fosters more informed decision-making in the optimization of solar cell technologies.

3.6. Optimized ACIGS for tandem solar cells

Recently, tandem perovskite-based solar cells (PSCs) have emerged as a dominant focus in photovoltaic research due to their high efficiency and low-cost processing compared to other solar cell technologies. From recent key research findings, we propose a detailed numerical investigation of two-terminal (2T) perovskite/ACIGS tandem solar cells using Silvaco TCAD tools, with an emphasis on their electrical and optical characteristics. Fig. 21(a) and (b) illustrate the tandem cell schematics. Two interconnection methods, band-to-band tunneling and series connection via ITO are employed to achieve high-efficiency tandem architectures, as shown in Fig. 21(a) and (b). In this tandem configuration, the optimized ACIGS cell serves as the bottom subcell, as illustrated in Fig. 21. The J_{sc} and maximum power point voltage (V_{mpp}) have been matched between the perovskite and ACIGS subcells to minimize internal losses, reduce current mismatches, and ensure efficient device operation [105]. The bottom ACIGS cell is illuminated only by low-energy photons [106]. Fig. 21(c) shows the simulated photogeneration rate as a function of position under AM 1.5 illumination, comparing a single-junction cell (blue line) and a tandem cell (red line). In the bottom subcell, no absorption occurs in the CdS and ZnO layers, as high-energy photons are already absorbed by the top perovskite cell. Under filtered illumination, the absorption in the space-charge region (SCR) of the ACIGS subcell is reduced, as shown in Fig. 21(c). The maximum J_{sc} increases with decreasing ACIGS bandgap, while the V_{oc} increases linearly with increasing bandgap. These characteristics have been optimized in our previous studies [105,106], where now we improved the tandem efficiencies for both interconnection configurations. Under filtered light, the J_{sc} curves shift downward due to the reduced spectrum. Additionally, the maximum achievable V_{oc} values decrease because of lower light intensity, which results in reduced quasi-Fermi level splitting [106]. The importance of the bottom cell's bandgap is influenced by the bandgap of the top cell. For higher top cell bandgaps, the bottom cell's maximum efficiency under filtered illumination is only slightly dependent on its bandgap. However, with higher-wavelength filters (corresponding to lower bandgap top cells), the achievable efficiency of the bottom cell increases. Some material and device parameters were derived from existing studies to align with experimentally fabricated models [105–114]. For an optimized tandem solar cell (TSC) with two junctions, the total tandem voltage and current can be expressed by applying Kirchhoff's law as:

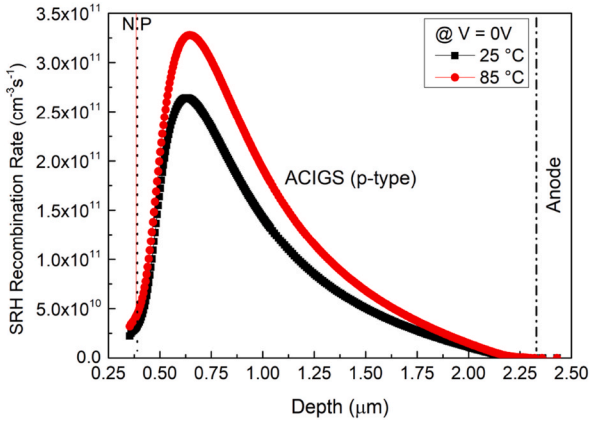

Fig. 17. SRH recombination rate across the cell for low/high temperatures.

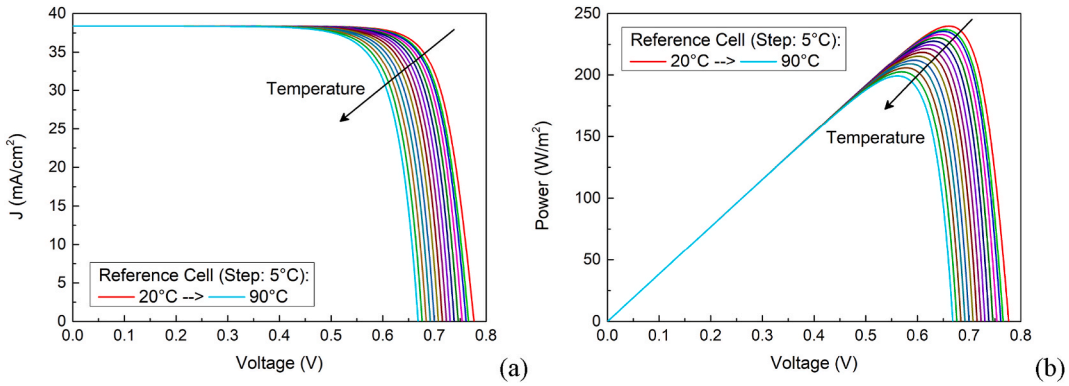

Fig. 18. (a) J–V characteristics (b) P–V characteristics at 100 mW/cm^2 intensity and different temperatures in the range from 20 to 90 °C for the ACIGS device under test (Sample with fixed bandgap for 1000 nm).

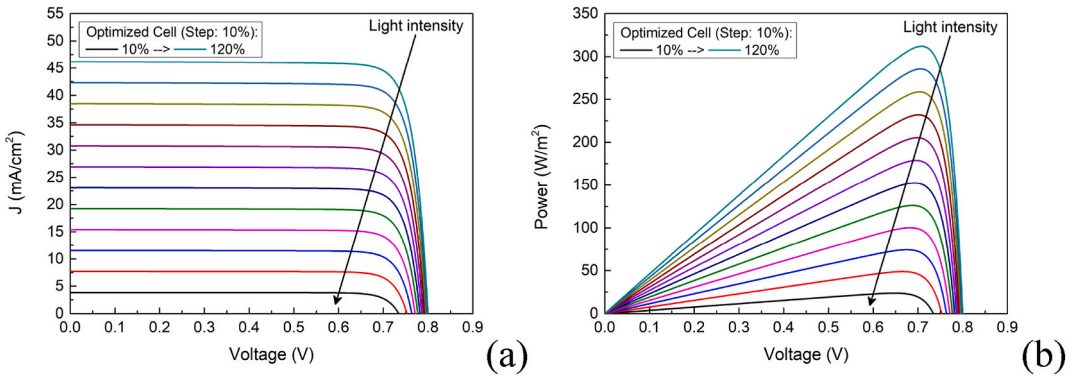

Fig. 19. (a) J–V characteristics (b) P–V characteristics at 25 °C temperature and different light intensities in the range from 10 to 120 % for the ACIGS device under test (Optimized sample with 200 nm notch depth).

$$J_{TSC} \approx J_{top,cell} \approx J_{bottom,cell} \tag{7}$$

$$V_{TSC} \approx V_{top,cell} + V_{int} + V_{bottom,cell} \tag{8}$$

Initially, the perovskite subcell was designed, tested, and calibrated based on experimental data reported in various research studies [107–114]. A new perovskite efficiency record of 26.7 % has been achieved, with an FF of 84.2 % and an V_{oc} of 1.193 V [79]. The FF improvement is attributed to enhanced interface passivation achieved by incorporating additives during the deposition process

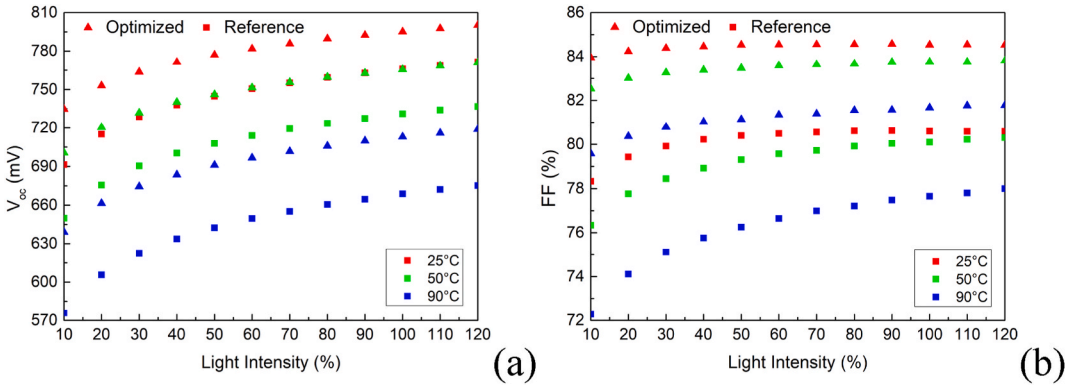

Fig. 20. V_{oc} and FF dependence on temperature and light intensity.

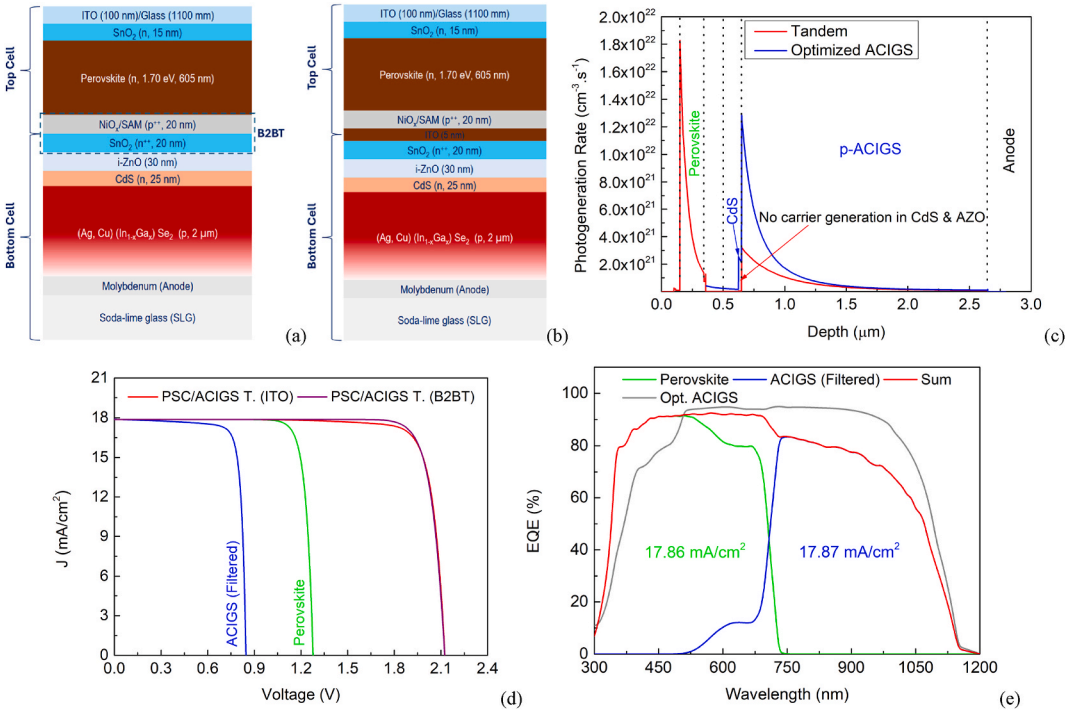

Fig. 21. (a) Cross-sectional view of the 2T perovskite/ACIGS tandem solar cell architecture with band-to-band tunneling (B2BT) interconnection. (b) Cross-sectional view of the 2T perovskite/ACIGS tandem solar cell with ITO interconnection. (c) Simulated photogeneration rates for the optimized ACIGS single-junction and 2T perovskite/ACIGS tandem solar cells under AM 1.5 illumination conditions. (d) J–V characteristics of the individual subcells and the integrated tandem devices. (e) External quantum efficiency (EQE) spectra of the subcells, their combined response, and the unfiltered ACIGS solar cell.

[115,116]. In our model, we have simplified the perovskite solar cell (PSC) structure, recognizing that additives can reduce recombination at the interfaces and improve carrier extraction toward the electrodes. The physical properties of the perovskite structure are provided in the supplementary material (Table S2). We assume no hysteresis effect in the PSC model. Fig. 21 illustrates the use of a NiO_x-MeO-2PACz self-assembled monolayer (SAM) (20 nm) as the hole transport layer (HTL). NiO_x can be doped with elements such as Li, Cu, and Ag to modify its electrical properties [115,116]. Ivona et al. demonstrated that doping NiO_x with Cu and passivating its surface with MeO-2PACz significantly reduces electron trapping, enhances hole extraction, and minimizes non-radiative recombination at the interface [116]. Single-crystal perovskites have been explored for their superior properties, including long diffusion lengths and low trap densities [117,118]. However, ACIGS solar cells still exhibit significantly less light-induced degradation compared to perovskite cells [117–121]. For the perovskite/ACIGS tandem configuration, we propose a perovskite subcell structure consisting of SnO_2 as the electron transport layer (ETL), deposited at 200 °C [111], a perovskite absorber layer with a 1.70 eV bandgap, and a NiO_x/SAM composite as the HTL [115]. The optical properties used in the simulation were obtained from the PV Lighthouse

database and from Rene's team [112,122]. Fig. 21(d) shows the J–V characteristics and Fig. 21(e) displays the external quantum efficiency (EQE) of the subcells and tandem structures. The J–V curves under forward scanning (from 0 V to 2.4 V) reveal power conversion efficiencies of 31.92 % and 32.39 % for tandem solar cells using ITO and band-to-band tunneling (B2BT) interconnections, respectively. These high efficiencies correspond to a short-circuit current density of 17.86 mA/cm^2, a fill factor exceeding 85.35 %, and an open-circuit voltage of 2.124 V. Table 4 summarizes the performance of these photovoltaic (PV) models in comparison with recent literature.

4. Conclusion

In this study, we conducted a comprehensive optimization of key parameters influencing the performance of ACIGS (Ag-doped Cu(In,Ga)Se_2) solar cells, focusing on the effects of deposition environment and techniques. Using advanced TCAD simulations, we analyzed parameters such as absorber thickness, dopant concentration, electron affinity, bulk defect density, and interface trap density. A calibrated device model based on experimental data was used to account for all relevant material properties and defect distributions. Our findings highlight that minimizing bulk and interface defects, primarily induced by deposition conditions, is crucial for enhancing both stability and performance. Under standard test conditions (AM1.5G, 25 °C), the reference and optimized ACIGS single-junction cells achieved power conversion efficiencies (PCEs) of 23.60 % and 25.80 %, respectively. In addition, under varying temperatures (20–90 °C) and illumination intensities (10–120 mW/cm^2), the optimized cell demonstrated significant improvements, including a 15 % enhancement in power temperature coefficient and a 22 % increase in voltage temperature coefficient. For tandem configurations, we paired the optimized ACIGS bottom cell with a perovskite top cell (bandgap ≈ 1.70 eV), resulting in PCEs of 31.92 % and 32.39 % for tandem devices using ITO and band-to-band tunneling (B2BT) interconnections, respectively, under AM1.5G illumination. These results are benchmarked against recent studies, providing valuable insights into advanced strategies and the physical behavior of high-efficiency tandem perovskite/ACIGS solar cells. This work contributes significantly to the design and optimization of high-performance photovoltaic systems and provides a solid foundation for future advancements in solar energy technology.

CRediT authorship contribution statement

Nour El I Boukortt: Writing – original draft, Software, Methodology, Investigation, Formal analysis. **Antonio Garcia Loureiro:** Writing – review & editing, Validation, Supervision, Resources, Conceptualization.

Consent to participate

Not Applicable.

Compliance with ethical standards

The manuscript is prepared per the journal's ethical standard. No Human Participants and/or Animals were involved while conducting this study.

Consent for publication

The authors have given consent for publication as per the journal policy.

Third-party material

No, all of the material is owned by the authors and/or no permissions are required.

Table 4
Performance parameters of the optimized models (* Certified).

PV Devices	J_{sc} (mA/cm^2)	V_{oc} (V)	FF (%)	η (%)	Ref.
Optimized Perovskite/ACIGS TSC (Interconnected via B2BT)	17.86	2.12	85.35	32.39	This work
Optimized Perovskite/ACIGS TSC (Interconnected via ITO)	17.86	2.12	84.11	31.92	This work
Top Perovskite	17.86	1.27	85.18	19.44	This work
Bottom ACIGS	17.87	0.84	83.03	12.55	This work
2T Perovskite/Cu(InGa)Se_2 TSC	17.20	1.85	83.87	26.69	[10]
2T Perovskite/AgCu(InGa)Se_2 TSC	18.04	2.03	79.25	29.14	[105]
2T Perovskite/Cu(InGa)Se_2 TSC	19.2	1.77	73	24.2*	[110]
2T Perovskite/Cu(InGa)Se_2 TSC	17.7	1.65	62	18.1	[123]
2T Perovskite/Cu(InGa)Se_2 TSC	–	–	–	29.9	[124]
2T Perovskite/Cu(InGa)Se_2 TSC	–	–	–	28.4	[125]

Funding

No funding was received to conduct this study.

Declaration of competing interest

The authors declare that they have no known competing financial interests or personal relationships that could have appeared to influence the work reported in this paper.

Acknowledgement

The authors declare no competing financial interests.

Appendix A. Supplementary data

Supplementary data to this article can be found online at https://doi.org/10.1016/j.micrna.2025.208220.

Data availability

No data was used for the research described in the article.

References

[1] P. Jackson, R. Wuerz, D. Hariskos, E. Lotter, W. Witte, M. Powalla, Effects of heavy alkali elements in Cu(In,Ga)Se 2 solar cells with efficiencies up to 22.6%, Phys. Status Solidi Rapid Res. Lett. 10 (8) (Jul. 2016) 583–586.
[2] T. Kato, J.-L. Wu, Y. Hirai, H. Sugimoto, V. Bermudez, Record efficiency for thin-film polycrystalline solar cells up to 22.9% achieved by Cs-treated Cu(in,Ga)(Se,S)2, IEEE J. Photovoltaics 9 (1) (Jan. 2019) 325–330.
[3] M. Nakamura, et al., Cd-free Cu(In,Ga)(Se,S)2 thin-film solar cell with record efficiency of 23.35, IEEE J. Photovoltaics 9 (2019) 1863–1867.
[4] J. Keller, et al., High-concentration silver alloying and steep back-contact gallium grading enabling copper indium gallium selenide solar cell with 23.6% efficiency, Nat. Energy (Feb. 2024) 1–12.
[5] N.E.I. Boukortt, S. Patanè, Y.M. Abdulraheem, Numerical investigation of CIGS thin-film solar cells, Sol. Energy 204 (Jul. 2020) 440–447.
[6] H. Sugimoto, et al., " T. High-performance near-stoichiometric Cu(In,Ga)Se_2 solar cells by sub-percent Ag-doping,", in: 29th PVSEC Conference, PVSEC, 2019, pp. 723–726.
[7] B. Namnuan, S. Chatraphorn, Improving the photovoltaic performance of CIGS solar cells with the modified 3-stage co-evaporation process, Mater. Sci. Semicond. Process. 179 (Aug. 2024) 108485.
[8] V.Q. Hoang, et al., Exploring the deposition pathway in the notch region of double-graded bandgap ACIGS solar cells, J. Sci. Adv. Mater. Devices 9 (1) (Mar. 2024) 100665.
[9] S. Jung, S. Ahn, J.H. Yun, J. Gwak, D. Kim, K. Yoon, Effects of Ga contents on properties of CIGS thin films and solar cells fabricated by co-evaporation technique, Curr. Appl. Phys. 10 (4) (Jul. 2010) 990–996.
[10] P. Procel, et al., Opto-electrical modelling and roadmap for 2T monolithic Perovskite/CIGS tandem solar cells, Solar Energy Mater. Solar Cells Solar Energy Mater Solar Cells 274 (Aug. 2024) 112975, 112975.
[11] T. Feurer, P. Reinhard, E. Avancini, B. Bissig, J. Löckinger, P. Fuchs, R. Carron, T.P. Weiss, J. Perrenoud, S. Stutterheim, S. Buecheler, Progress in thin film CIGS photovoltaics–Research and development, manufacturing, and applications, Prog. Photovoltaics Res. Appl. 25 (7) (2017) 645–667.
[12] Sarallah Hamtaei, G. Brammertz, Jef Poortmans, B. Vermang, "A review on barrier layers used in flexible stainless-steel based CIGS photovoltaic devices,", Npj Flex. Electr. 7 (1) (Aug. 2023).
[13] I. Repins, et al., 19·9%-efficient ZnO/CdS/CuInGaSe2 solar cell with 81·2% fill factor, Prog. Photovoltaics Res. Appl. 16 (3) (Feb. 2008) 235–239.
[14] X. He, et al., The role of oxygen doping on elemental intermixing at the PVD-CdS/Cu (InGa)Se_2 heterojunction, Prog. Photovoltaics Res. Appl. 27 (3) (Dec. 2018) 255–263.
[15] M.-G. Tsai, et al., Annealing effect on the properties of Cu(In0.7Ga0.3)Se2 thin films grown by femtosecond pulsed laser deposition, J. Am. Ceram. Soc. 96 (2013) 2419–2423.
[16] J.-H. Park, et al., The deposition of thin films of CuME2 by CVD techniques (M = In, Ga and E = S, Se), J. Mater. Chem. 13 (8) (Jan. 2003) 1942, 1942.
[17] I.H. Choi, D.H. Lee, Preparation of CuIn1−xGaxSe2 films by metalorganic chemical vapor deposition using three precursors, Thin Solid Films 515 (11) (Apr. 2007) 4778–4782.
[18] M. Venkatachalam, M.D. Kannan, S. Jayakumar, R. Balasundaraprabhu, N. Muthukumarasamy, Effect of annealing on the structural properties of electron beam deposited CIGS thin films, Thin Solid Films 516 (20) (Aug. 2008) 6848–6852.
[19] T. Nakada, M. Mizutani, Y. Hagiwara, A. Kunioka, High-efficiency Cu(In,Ga)Se2 thin-film solar cells with a CBD-ZnS buffer layer, Sol. Energy Mater. Sol. Cell. 67 (1–4) (Mar. 2001) 255–260.
[20] A.E. Delahoy, L. Chen, M. Akhtar, B. Sang, S. Guo, New technologies for CIGS photovoltaics, Sol. Energy 77 (6) (Dec. 2004) 785–793.
[21] K. Kushiya, et al., Progress in large-area Cu(InGa)Se2-based thin-film modules with a Zn(O,S,OH)x buffer layer, Sol. Energy Mater. Sol. Cell. 67 (1–4) (Mar. 2001) 11–20.
[22] C. Jeong, et al., Examination of suitable bandgap grading of Cu(InGa)Se2 bottom absorber layers for tandem cell application, Phys. Status Solidi 218 (10) (Mar. 2021).
[23] D. Colombara, et al., Sodium enhances indium-gallium interdiffusion in copper indium gallium diselenide photovoltaic absorbers, Nat. Commun. 9 (1) (Feb. 2018).
[24] P. Chelvanathan, et al., Effects of RF magnetron sputtering deposition process parameters on the properties of molybdenum thin films, Thin Solid Films 638 (Sep. 2017) 213–219.
[25] M. Pepper, "Metal-semiconductor contacts," Phys. Technol., vol. 5, no. 4, pp. 223–223, Jan. 197.
[26] H.B. Michaelson, The work function of the elements and its periodicity, J. Appl. Phys. 48 (11) (Nov. 1977) 4729–4733.
[27] A. Janotti, C.G. Van de Walle, Fundamentals of zinc oxide as a semiconductor, Rep. Prog. Phys. 72 (12) (Oct. 2009) 126501.

[28] A. Janotti, C.G. Van de Walle, Native point defects in ZnO, Phys. Rev. B 76 (16) (Oct. 2007).
[29] A.B.F. Martinson, J.W. Elam, J.T. Hupp, M.J. Pellin, ZnO nanotube based dye-sensitized solar cells, Nano Lett. 7 (8) (Jun. 2007) 2183–2187.
[30] T. Ruf, S. Repp, J. Urban, R. Thomann, E. Erdem, Competing effects between intrinsic and extrinsic defects in pure and Mn-doped ZnO nanocrystals, J. Nanoparticle Res. 18 (5) (Apr. 2016).
[31] B. Ehrler, et al., Preventing interfacial recombination in colloidal quantum dot solar cells by doping the metal oxide, ACS Nano 7 (5) (Apr. 2013) 4210–4220.
[32] Agnieszka Kawska, P. Duchstein, O. Hochrein, D. Zahn, Atomistic mechanisms of ZnO aggregation from ethanolic solution: ion association, proton transfer, and self-organization, Nano Lett. 8 (8) (Jun. 2008) 2336–2340.
[33] M. Wu, D. Sun, C. Tan, X. Tian, Y. Huang, Al-doped ZnO monolayer as a promising transparent electrode material: a first-principles study, Materials 10 (4) (Mar. 2017) 359.
[34] H. Liu, V. Avrutin, N. Izyumskaya, Ü. Özgür, H. Morkoç, Transparent conducting oxides for electrode applications in light emitting and absorbing devices, Superlattice. Microst. 48 (5) (Nov. 2010) 458–484.
[35] A.R. Kaul, O. Yu Gorbenko, A.N. Botev, L.I. Burova, MOCVD of pure and Ga-doped epitaxial ZnO, Superlattice. Microst. 38 (4–6) (Oct. 2005) 272–282.
[36] M. Snure, A. Tiwari, Structural, electrical, and optical characterizations of epitaxial Zn1−xGaxO films grown on sapphire (0001) substrate, J. Appl. Phys. 101 (12) (Jun. 2007).
[37] A. Klein, et al., Transparent conducting oxides for photovoltaics: manipulation of Fermi level, work function and energy band alignment, Materials 3 (11) (Nov. 2010) 4892–4914.
[38] J. Ramanujam, U.P. Singh, Copper indium gallium selenide based solar cells – a review, Energy Environ. Sci. 10 (6) (2017) 1306–1319.
[39] A. El Manouni, et al., Effect of aluminium doping on zinc oxide thin films grown by spray pyrolysis, Superlattice. Microst. 39 (1–4) (Jan. 2006) 185–192.
[40] K. Liu, M. Sakurai, M. Liao, M. Aono, Giant improvement of the performance of ZnO nanowire photodetectors by Au nanoparticles, J. Phys. Chem. C 114 (46) (Oct. 2010) 19835–19839.
[41] A.K. Pradhan, K. Zhang, G.B. Loutts, U.N. Roy, Y. Cui, A. Burger, Structural and spectroscopic characteristics of ZnO and ZnO:Er^{3+}nanostructures, J. Phys. Condens. Matter 16 (39) (Sep. 2004) 7123–7129.
[42] S.A. Mahmoud, A.A. Ibrahim, A.S. Riad, Physical properties of thermal coating CdS thin films using a modified evaporation source, Thin Solid Films 372 (1–2) (Sep. 2000) 144–148.
[43] S.J. Castillo, et al., Structural, optical and electrical characterization of In/CdS/glass thermally annealed system, Thin Solid Films 373 (1–2) (Sep. 2000) 10–14.
[44] K.L. Choy, B. Su, Growth behavior and microstructure of CdS thin films deposited by an electrostatic spray assisted vapor deposition (ESAVD) process, Thin Solid Films 388 (1–2) (Jun. 2001) 9–14.
[45] Han Fu, Hong Liu, Wenzhong Shen, A composite CdS thin film/TiO 2 nanotube structure by ultrafast successive electrochemical deposition toward photovoltaic application, Nanoscale Res. Lett. 9 (2014) 1–13.
[46] H. Ashour, F. El Akkad, Trap levels in RF sputtered CdS thin films, Phys. Status Solidi 184 (1) (Mar. 2001) 175–178.
[47] A. Ashok, G. Regmi, A. Romero-Núñez, M. Solís-López, S. Velumani, H. Castaneda, Comparative studies of CdS thin films by chemical bath deposition techniques as a buffer layer for solar cell applications 31 (10) (Feb. 2020) 7499–7518.
[48] J. Hiie, K. Muska, V. Valdna, V. Mikli, A. Taklaja, A. Gavrilov, Thermal annealing effect on structural and electrical properties of chemical bath-deposited CdS films, Thin Solid Films 516 (20) (Aug. 2008) 7008–7012.
[49] A.I. Oliva-Avilés, R. Patiño, A.I. Oliva, CdS films deposited by chemical bath under rotation, Appl. Surf. Sci. 256 (20) (Aug. 2010) 6090–6095.
[50] J. McAleese, P. O'Brien, D.J. Otway, A novel simple process for the deposition of thin films of CuInSe2 by MOCVD, Chem. Vap. Depos. 4 (3) (May 1998) 94–96.
[51] M. Cao, Y. Sun, J. Wu, X. Chen, N. Dai, Effects of cadmium salts on the structure, morphology and optical properties of acidic chemical bath deposited CdS thin films, J. Alloys Compd. 508 (2) (Oct. 2010) 297–300.
[52] S.-Y. Lee, et al., A general guide for adsorption of cadmium sulfide (CdS) quantum dots by successive ionic layer adsorption and reaction (SILAR) for efficient CdS-sensitized photoelectrochemical cells, Appl. Surf. Sci. 589 (Feb. 2022) 152898, 152898.
[53] H.K. Jun, M.A. Careem, A.K. Arof, Quantum dot-sensitized solar cells—perspective and recent developments: a review of Cd chalcogenide quantum dots as sensitizers, Renew. Sustain. Energy Rev. 22 (Jun. 2013) 148–167.
[54] Ben Chu Van, et al., Waste- and Cd-free inkjet-printed Zn(O,S) buffer for Cu(in,Ga)$(S,Se)_2$ thin-film solar cells, ACS Appl. Mater. Interfaces 13 (11) (Mar. 2021) 13009–13021.
[55] Marius Franckevičius, et al., Efficiency improvement of superstrate CZTSSe solar cells processed by spray pyrolysis approach, Sol. Energy 185 (Jun. 2019) 283–289.
[56] M.E. Sonawane, et al., MoS2 augmentation in CZTS solar cells: detailed experimental and simulation analysis, Nano-Struct. Nano-Objects 39 (Jul. 2024) 101268.
[57] R. Scheer, L. Messmann-Vera, R. Klenk, H.-W. Schock, On the role of non-doped ZnO in CIGSe solar cells, Prog. Photovoltaics Res. Appl. 20 (6) (Nov. 2011) 619–624.
[58] Jean-Pierre Colinge and C. A, Colinge, Physics of Semiconductor Devices, Springer, Boston, Mass., 2006.
[59] A.S. Najm, et al., Mechanism and principle of doping: realizing of silver incorporation in CdS thin film via doping concentration effect, RSC Adv. 12 (46) (2022) 29613–29626.
[60] F.J. Willars-Rodríguez, I.R. Chávez-Urbiola, M.A. Hernández-Landaverde, P. Vorobiev, R. Ramírez-Bon, Y.V. Vorobiev, Effects of tin-doping on cadmium sulfide (CdS:Sn) thin-films grown by light-assisted chemical bath deposition process for solar photovoltaic cell, Thin Solid Films 653 (May 2018) 341–349.
[61] N. Maticiuc, J. Hiie, T. Raadik, A. Graf, A. Gavrilov, The role of Cl in the chemical bath on the properties of CdS thin films, Thin Solid Films 535 (May 2013) 184–187.
[62] S. Chandramohan, A. Kanjilal, S.N. Sarangi, S. Majumder, R. Sathyamoorthy, T. Som, Implantation-assisted Co-doped CdS thin films: structural, optical, and vibrational properties, J. Appl. Phys. 106 (6) (Sep. 2009).
[63] P.J. Sebastian, p-type CdS thin films formed byinsituCu doping in the chemical bath, Appl. Phys. Lett. 62 (23) (Jun. 1993) 2956–2958.
[64] O. Portillo-Moreno, et al., Growth of CdS:Cu nanocrystals by chemical synthesis, J. Electrochem. Soc. 153 (10) (2006) 926–930.
[65] Y. Sanchez, et al., High VOC Cu2ZnSnSe4/CdS:Cu Based Solar Cell: Evidences of a Metal-Insulator-Semiconductor (MIS) Type Hetero-Junction, Jun. 2014.
[66] K.K. Challa, E. Magnone, E.-T. Kim, Highly photosensitive properties of CdS thin films doped with boron in high doping levels, Mater. Lett. 85 (Jul. 2012) 135–137.
[67] H. Khallaf, G. Chai, O. Lupan, L. Chow, S. Park, A. Schulte, Investigation of aluminium and indiumin situdoping of chemical bath deposited CdS thin films, J. Phys. Appl. Phys. 41 (18) (Aug. 2008) 185304.
[68] S. Alhammadi, et al., Effect of Gallium doping on CdS thin film properties and corresponding Cu(InGa)Se2/CdS:Ga solar cell performance, Thin Solid Films 660 (Aug. 2018) 207–212.
[69] S.M. Sze, Kwok Kwok Ng, Physics of Semiconductor Devices, Wiley-Interscience, Hoboken, Nj, 2006.
[70] M. Ristova, Silver-doped CdS films for PV application, Sol. Energy Mater. Sol. Cell. 53 (1–2) (May 1998) 95–102.
[71] M. Ristova, M. Ristov, P. Tosev, M. Mitreski, Silver doping of thin CdS films by an ion exchange process, Thin Solid Films 315 (1–2) (Mar. 1998) 301–304.
[72] Chandramohan, T. Strache, S.N. Sarangi, R. Sathyamoorthy, T. Som, Influence of implantation induced Ni-doping on structural, optical, and morphological properties of nanocrystalline CdS thin films, Mater. Sci. Eng., B 171 (1–3) (Jul. 2010) 16–19.
[73] S. Aksu, et al., Structural, optical and magnetic properties of Mn diffusion-doped CdS thin films prepared by vacuum evaporation 130 (1–2) (Oct. 2011) 340–345.
[74] H. Khallaf, G. Chai, O. Lupan, L. Chow, S. Park, A. Schulte, Characterization of gallium-doped CdS thin films grown by chemical bath deposition, Appl. Surf. Sci. 255 (7) (Jan. 2009) 4129–4134.
[75] R. Mariappan, V. Ponnuswamy, M. Ragavendar, D. Krishnamoorthi, C. Sankar, The effect of annealing temperature on structural and optical properties of undoped and Cu doped CdS thin films, Optik 123 (12) (Jun. 2012) 1098–1102.

[76] Y. Kashiwaba, T. Komatsu, M. Nishikawa, Y. Ishikawa, K. Segawa, Y. Hayasi, X-Ray diffraction studies of p-CdS:Cu thin films, Thin Solid Films 408 (1–2) (Mar. 2002) 43–50.
[77] S.R. Ferrá-González, et al., Optical and structural properties of CdS thin films grown by chemical bath deposition doped with Ag by ion exchange, Optik 125 (4) (Nov. 2013) 1533–1536.
[78] H. Hahn, G. Frank, W. Klingler, A. Meyer, Georg Störger, Untersuchungen ber ternre Chalkogenide. V.ber einige ternre Chalkogenide mit Chalkopyritstruktur, Z. Anorg. Allg. Chem. 271 (3–4) (Feb. 1953) 153–170.
[79] National Renewable Energy Laboratory, Best Research-Cell Efficiency Chart | Photovoltaic Research, NREL, 2025. Nrel.gov, https://www.nrel.gov/pv/cell-efficiency.html.
[80] M.A. Green, Third generation photovoltaics: solar cells for 2020 and beyond, Phys. E Low-dimens. Syst. Nanostruct. 14 (1–2) (Apr. 2002) 65–70.
[81] W. Shockley, H.J. Queisser, Detailed balance limit of efficiency of p-n junction solar cells, J. Appl. Phys. 32 (3) (1961) 510–519.
[82] ATLAS User's Manual Device Simulation Software, 2016. Silvaco International Ltd.,Santa Clara, USA.
[83] T. Klinkert, M. Jubault, Frédérique Donsanti, D. Lincot, Jean-François Guillemoles, Differential in-depth characterization of co-evaporated Cu(In,Ga)Se2 thin films for solar cell applications, Thin Solid Films 558 (Feb. 2014) 47–53.
[84] Xiaoyu Lv, Z. Zheng, M. Zhao, H. Wang, D. Zhuang, Investigation on preparation and performance of high Ga CIGS absorbers and their solar cells, Materials 16 (7) (Mar. 2023) 2806, 2806.
[85] Shih Chen Chen, et al., Growth and characterization of Cu(In,Ga)Se2 thin films by nanosecond and femtosecond pulsed laser deposition, Nanoscale Res. Lett. 9 (1) (Jun. 2014).
[86] M. Kaelin, D. Rudmann, A.N. Tiwari, Low cost processing of CIGS thin film solar cells, Sol. Energy 77 (6) (Dec. 2004) 749–756.
[87] S.-C. Chen, et al., A comprehensive study of one-step selenization process for Cu(In1−x Ga x)Se2 thin film solar cells, Nanoscale Res. Lett. 12 (1) (Mar. 2017).
[88] J. Lindahl, C. Hägglund, J.T. Wätjen, M. Edoff, T. Törndahl, The effect of substrate temperature on atomic layer deposited zinc tin oxide, Thin Solid Films 586 (Jul. 2015) 82–87.
[89] J. Lindahl, J. Keller, O. Donzel-Gargand, P. Szaniawski, M. Edoff, T. Törndahl, Deposition temperature induced conduction band changes in zinc tin oxide buffer layers for Cu(In,Ga)Se2 solar cells, Sol. Energy Mater. Sol. Cell. 144 (Jan. 2016) 684–690.
[90] D. Bae, A statistical approach to scaling up of CIGS PV cells: quantitative analysis of composition uniformity within and between the samples, Mater. Sci. Semicond. Process. 164 (Sep. 2023) 107626.
[91] A. Duchatelet, Elénore Letty, J.S. Jaime-Ferrer, P. Grand, F. Mollica, Negar Naghavi, The impact of reducing the thickness of electrodeposited stacked Cu/In/Ga layers on the performance of CIGS solar cells, Sol. Energy Mater. Sol. Cell. 162 (Apr. 2017) 114–119.
[92] S.-N. Zhang, S.-H. Wei, A. Zunger, Hiroshi Katayama-Yoshida, Defect physics of theCuInSe2chalcopyrite semiconductor 57 (16) (Apr. 1998) 9642–9656.
[93] Y. Sun, et al., Review on alkali element doping in Cu(in,Ga)Se 2 thin films and solar cells, Engineering 3 (4) (Aug. 2017) 452–459.
[94] D. Rudmann, et al., Efficiency enhancement of Cu(In,Ga)Se2 solar cells due to post-deposition Na incorporation, Appl. Phys. Lett. 84 (7) (Feb. 2004) 1129–1131.
[95] C.M. Sutter-Fella, et al., Sodium assisted sintering of chalcogenides and its application to solution processed $Cu_2ZnSn(S,Se)_4$ thin film solar cells, Chem. Mater. 26 (3) (Jan. 2014) 1420–1425.
[96] D. Colombara, et al., Deliberate and accidental gas-phase alkali doping of chalcogenide semiconductors: Cu(in,Ga)Se2, Sci. Rep. 7 (1) (Feb. 2017).
[97] U. Rau, et al., Oxygenation and air-annealing effects on the electronic properties of Cu(In,Ga)Se2 films and devices, J. Appl. Phys. 86 (1) (Jul. 1999) 497–505.
[98] H. Rodriguez-Alvarez, et al., Real-time study of Ga diffusion processes during the formation of Cu(In,Ga)Se2: the role of Cu and Na content, Sol. Energy Mater. Sol. Cell. 116 (May 2013) 102–109.
[99] D. Colombara, K. Conley, M. Malitckaya, Hannu Pekka Komsa, M.J. Puska, The fox and the hound: in-depth and in-grain Na doping and Ga grading in Cu(In,Ga)Se_2 solar cells, J. Mater. Chem. A 8 (14) (Jan. 2020) 6471–6479.
[100] R.V. Forest, E. Eser, B.E. McCandless, J.G. Chen, R.W. Birkmire, Reversibility of (Ag,Cu)(In,Ga)Se2 electrical properties with the addition and removal of Na: role of grain boundaries, J. Appl. Phys. 117 (11) (Mar. 2015).
[101] Soňa Uličná, et al., Sodium doping of solution-processed amine-thiol based CIGS solar cells by thermal evaporation of NaCl, Prog. Photovoltaics Res. Appl. 29 (5) (Mar. 2021) 546–557.
[102] Md F. Rahman, et al., A qualitative design and optimization of CIGS-based solar cells with Sn2S3 back surface field: a plan for achieving 21.83 % efficiency, Heliyon 9 (12) (Dec. 2023) e22866.
[103] N.E.I. Boukortt, S. Patanè, M. Adouane, R. AlHammadi, Numerical optimization of ultrathin CIGS solar cells with rear surface passivation, Sol. Energy 220 (May 2021) 590–597.
[104] A. G. Loureiro Nour, A. Abushattal, Efficiency improvement of ultrathin CIGS solar cells, Sol. Energy 282 (Sep. 2024) 112935, 112935.
[105] Nour Boukortt, A.G. Loureiro, Johan Lauwaert, Optimizing thin-film tandem solar cells: the impact of bandgap grading in ACIGS subcell on performance, IEEE Trans. Electron. Dev. (Jan. 2025) 1–9.
[106] N.E.I. Boukortt, A.G. Loureiro, O.A. Almutairi, Numerical analysis of Ga gradient effects in ACIGS absorbers for high-efficiency tandem solar cells, Opt. Quant. Electron. 57 (3) (Mar. 2025).
[107] A.M. Bothwell, et al., Large-area (Ag,Cu)(In,Ga)Se2 thin-film solar cells with increased bandgap and reduced voltage losses realized with bulk defect reduction and front-grading of the absorber bandgap, Sol. RRL 6 (8) (Apr. 2022).
[108] H.A. Yetkin, et al., Decay mechanisms in CdS-buffered Cu(In,Ga)Se_2 thin-film solar cells after exposure to thermal stress: understanding the role of Na, Prog. Photovoltaics Res. Appl. 29 (9) (May 2021) 1034–1053.
[109] H. Chen, et al., Unraveling the influence of interface defects on antimony trisulfide solar cells, J. Energy Chem. 78 (Nov. 2022) 262–267.
[110] M. Jošt, et al., Perovskite/CIGS tandem solar cells: from certified 24.2% toward 30% and beyond, ACS Energy Lett. (Mar. 2022) 1298–1307.
[111] Y. Kuang, et al., Low-temperature plasma-assisted atomic-layer-deposited SnO2 as an electron transport layer in planar perovskite solar cells, ACS Appl. Mater. Interfaces 10 (36) (Aug. 2018) 30367–30378.
[112] J. Wang, V. Zardetto, K. Datta, D. Zhang, M.M. Wienk, R.A.J. Janssen, 16.8% Monolithic all-perovskite triple-junction solar cells via a universal two-step solution process, Nat. Commun. 11 (1) (Oct. 2020).
[113] Q. Zhang, X. Chen, E.L. Lim, L. Shi, Z. Wei, Advancing all-perovskite two-terminal tandem solar cells: optimization of wide- and narrow-bandgap perovskites and interconnecting layers, Energy Environ. Sci. 18 (2025) 3060–3084.
[114] Z. Wei, et al., Surpassing 90% Shockley–Queisser VOC limit in 1.79 eV wide-bandgap perovskite solar cells using bromine-substituted self-assembled monolayers, Energy Environ. Sci. 18 (4) (2025) 1847–1855.
[115] H. Chen, et al., Regulating surface potential maximizes voltage in all-perovskite tandems, Nature 620 (7973) (Nov. 2022). E15-E15.
[116] Ivona Kafedjiska, et al., Advanced characterization and optimization of NiOx:Cu-SAM hole-transporting Bi-layer for 23.4% efficient monolithic Cu(in,Ga)Se2-perovskite tandem solar cells, Adv. Funct. Mater. 33 (34) (May 2023) 2302924.
[117] Y. Cho, H.R. Jung, W. Jo, Halide perovskite single crystals: growth, characterization, and stability for optoelectronic applications, Nanoscale 14 (26) (2022) 9248–9277.
[118] W. Chi, S.K. Banerjee, Comparison and integration of CuInGaSe and perovskite solar cells, J. Energy Chem. 78 (Mar. 2023) 463–475.
[119] L. Tian, et al., Divalent cation replacement strategy stabilizes wide-bandgap perovskite for Cu(In,Ga)Se2 tandem solar cells, Nat. Photonics (Feb. 2025).
[120] J. Tao, et al., Suppressing non-radiative recombination for efficient and stable perovskite solar cells, Energy Environ. Sci. 18 (Jan. 2024) 509–544.
[121] L. Zang, C. Zhao, X. Hu, J. Tao, S. Chen, J. Chu, Emerging trends in electron transport layer development for stable and efficient perovskite solar cells, Small 20 (26) (Apr. 2024) 2400807.
[122] https://www.pvlighthouse.com.au/refractive-index-library.

[123] J. Zheng, et al., Efficient flexible monolithic perovskite–CIGS tandem solar cell on conductive steel substrate, ACS Energy Lett. (Mar. 2024) 1545–1547.
[124] H. Liang, et al., 29.9%-efficient, commercially viable perovskite/CuInSe2 thin-film tandem solar cells, Joule 7 (12) (Nov. 2023) 2859–2872.
[125] X. Liu, et al., Over 28% efficiency perovskite/Cu(InGa)Se2 tandem solar cells: highly efficient sub-cells and their bandgap matching, Energy Environ. Sci. 16 (11) (Jan. 2023) 5029–5042.